This is the accepted version of the article published in the final form in Journal of Materials Chemistry A vol. 8, issue 17, pages 8752–8760, in 2020 by the Royal Society of Chemistry at DOI: 10.1039/D0TA03162C.

https://doi.org/10.1039/D0TA03162C

ARTICLE

Synthesis of Metal-Free Lightweight Materials with Sequence-Encoded Properties

Received 00th January 20xx,
Accepted 00th January 20xx

DOI: 10.1039/x0xx00000x

Adi Azoulay[a], Jesús Barrio[a], Jonathan Tzadikov[a], Michael Volokh[a], Josep Albero[b], Christel Gervais[c], Pilar Amo-Ochoa[d], Hermenegildo García[b], Félix Zamora[d,e], Menny Shalom*[a]

A high-temperature solid-state synthesis is a widespread tool for the construction of metal-free materials, owing to its simplicity and scalability. However, no method is currently available for the synthesis of metal-free materials, which enables control over the atomic ratio and spatial organization of several heteroatoms. Here we report a general and large-scale synthesis of phosphorus-nitrogen-carbon (PNC) materials with highly controllable elemental composition and structural, electronic, and thermal stability properties. To do so, we designed four different crystals consisting of melamine and phosphoric acid with different monomers sequences as the starting precursors. The monomer sequence of the crystals is preserved upon calcination (up to 800 °C) to an unprecedented degree, which leads to precise control over the composition of the final PNC materials. The latter exhibit a remarkable stability up to 970 °C in air, positioning them as sustainable, lightweight supports for catalysts in high-temperature reactions as well as halogen-free fire-retardant materials.

Introduction

Metal-free materials have emerged as a new class of materials with a wide range of applications, spanning catalysis, batteries, fuel cells, and other energy-related applications thanks to their tunable electronic, structural, and catalytic properties, as well as their low-price.[1] The insertion of heteroatoms within carbon matrices is a versatile tool for tuning their conductivity, optical, and electronic properties, encompassing semimetal-like properties, semiconductors, and insulators, depending on the atomic size and electronegativity of the doping element compared to carbon, as well as the relative concentration of heteroatom.[2] From similar considerations, when three elements (namely, phosphorus, nitrogen, and carbon, i.e., PNC) serve as the building blocks, many new materials ranging from polyphosphazenes to phosphorous- and nitrogen-doped carbon can be synthesized, resulting in a wide spectrum of exciting properties.[3–5] For example, integration of a P-N group in carbon frameworks dramatically enhances their stability at high temperatures due to the formation of strong P-N bonds in the scaffold.[6] Furthermore, P and N alter the materials' electrical and thermal conductivity. Along with their excellent thermal stability, tunable composition, and low density, polyphosphazenes could be convenient candidates as heterogeneous catalysts or catalyst supports. Typical industrial catalyst supports are based on metal oxides, such as alumina-silicates, among others, being a source of contamination once the catalysts are deactivated. However, the polyphosphazenes presented herein show environmentally friendly combustion by-products. On the other hand, they could offer the possibility to act also as halogen-based flame-retardants materials.[7] Moreover, the dissimilar electronegativity leads to tunable optical and electrical properties, enabling their utilization in various research fields.[8,9] However, up to today, the design of these materials at high temperature is highly challenging due to the complex solid-state reactions, which do not allow control over the atomic composition and organization within the scaffold. The high temperature together with the solid-solid interaction of two or more monomers make it almost impossible to precisely control the synthesis path and the final composition and properties of PNC materials. Recently, we and others have demonstrated the utilization of supramolecular aggregates and crystals as reactants for the synthesis of carbon nitride (CN) polymers.[10–12] This approach permits the synthesis of CN polymers with good control over their structural, chemical, and electronic properties thanks to the imprint of the molecular order[13] from the precursor-level to the final CN.[14] Therefore, this approach can potentially provide the capability to rationally synthesize any framework with a controlled elemental composition, including with structurally targeted insertion of heteroatoms, toward its application in a given field.

[a] Department of Chemistry and Ilse Katz Institute for Nanoscale Science and Technology, Ben-Gurion University of the Negev, Beer-Sheva 8410501, Israel. E-mail: mennysh@bgu.ac.il
[b] Instituto Universitario Mixto de Tecnología Química (UPV-CSIC), Universitat Politècnica de València, Avda. de los Narajos s/n, 46022, Valencia, Spain.
[c] Sorbonne Université, College de France, Laboratoire de Chimie de la Matière Condensée de Paris (LCMCP), UMR CNRS 7574 4 place Jussieu, 75252 Paris cedex 05, France.
[d] Departamento de Química Inorgánica, Institute for Advanced Research in Chemical Sciences (IAdChem) and Condensed Matter Physics Center (IFIMAC). Universidad Autónoma de Madrid, E-28049 Madrid, Spain.
[e] Instituto Madrileño de Estudios Avanzados en Nanociencia (IMDEA-Nanociencia). Cantoblanco E-28049 Madrid, Spain.
Electronic Supplementary Information (ESI) available: [details of any supplementary information available should be included here]. See DOI: 10.1039/x0xx00000x

Here we show a general, simple, and large-scale synthesis of phosphorus-nitrogen-carbon (PNC) materials with highly tunable elemental composition as well as structural, electronic, and thermal stability properties. To do so, we designed and prepared four phosphoric acid–melamine monocrystalline materials with different monomers sequence and spatial organization, prepared through slow evaporation of an aqueous solution of the reaction monomers. Upon calcination up to 800 °C, well-organized PNC materials with tunable elemental composition as well as controlled properties were achieved. Specifically, this approach allows a precise control over phosphorus amount ranging from 10 to 50 wt. %, much higher than the standard inclusion of phosphorus in CN frameworks by other means, which typically results in trace doping. Their designed elemental and structural morphology endow the direct measurements of the materials' conductivity and thermal stability to oxidation, demonstrating remarkable stability under harsh reaction conditions, as the materials are stable up to 970 °C under air.

Results and discussion

Four different phosphoric acid–melamine (PA_xM_y, where *x*:*y* is the initial molar ratio) monocrystalline materials were designed by slow evaporation of an aqueous solution of the starting monomers in different molar ratios, ranging from 2:1 to 1:4. (See experimental section for further details). Single crystal X-ray diffraction (SC-XRD) indicates the strong dependency of the crystal structure and cell parameters for each one of the crystals with the starting molar ratio, leading to different crystals with altered monomers order (Table S1). The material prepared with the highest amount of phosphoric acid (PA_2M_1) afforded a melaminium ortophosphate structure with triclinic crystal system,[15] while decreasing the phosphoric acid relative amount to a 1:1 ratio resulted in an unprecedented PA_1M_1 crystal structure, where a diprotonated melamine unit is hydrogen-bonded to a phosphoric acid molecule through an endocyclic nitrogen atom (Fig. 1a, Table S2). The most relevant distances and angles are displayed in Table S1. Further alteration of the PA:M ratio to 1:2 produced another structure where the melamine unit is connected by a hydrogen bond to a water molecule, while another two water molecules are connected to a single phosphoric acid molecule that is linked to the second melamine unit in the structure.[16] The analysis of PA_1M_4 revealed a polycrystalline nature with two different crystal structures, corresponding to PA_1M_2 and to pure melamine (Fig. S1).

The structures of the single crystals are further supported by powder X-ray diffraction (P-XRD) pattern analysis and Fourier transform infra-red (FTIR) spectroscopy measurements of all materials, which are provided in Fig. S2. Both XRD and FTIR show the ordered hydrogen bonds interactions between the materials' precursors (full discussion is provided in ESI). Optical microscopy images (Fig. S3a–e) of single crystals from the different materials show parallelogram-shaped structures for melamine, PA_1M_4, and PA_1M_2, while increasing the phosphoric acid-to-melamine molar ratio in the synthesis leads to thinner and more compressed needle-like structure. The images

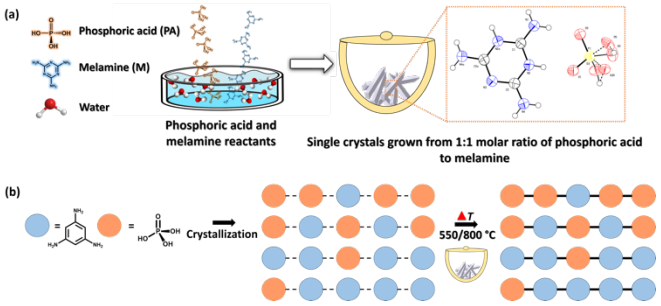

Fig. 1 (a) Synthesis of PA_1M_1 single crystal and its corresponding structure. (b) A general illustration of PNC_x materials synthesis.

obtained for PA_1M_4, the crystalline material with the lowest P wt. %, (Fig. S3b) suggest a superposition of morphologies of both PA_1M_2 and melamine single crystals.

^{31}P MAS spectra of PA_2M_1, PA_1M_1, PA_1M_2, and PA_1M_4 crystals (Fig. S4a) show signals around 0 ppm, typical of PO_4 environments. Moreover, as expected, signals are similar for PA_1M_2 and PA_1M_4. Calculated values for PA_1M_2 and PA_2M_1 (1.3 and 0.3 ppm) are in excellent agreement with experimental ones (1.4 and -0.1 ppm). In the case of PA_1M_1, the spectrum shows 3 peaks at 3.9, 1.3 and -0.8 ppm, which are not expected according to the crystalline structure with only one phosphorus site (calculated at 2.8 ppm). This suggests the presence of some disorder or defects. ^{13} CP MAS spectra of the crystals (Fig. S4b) show two signals around 165 and 158 ppm corresponding in PA_2M_1, PA_1M_2, and PA_1M_4 to (i) carbons linked to two deprotonated nitrogens in the cycle and (ii) carbons linked to one protonated and one deprotonated nitrogen in the cycle, respectively, in good agreement with the relative intensities and calculated values. In the case of PA_1M_1, carbon C2 is expected around 156 ppm according to calculations and in agreement with similar environments in PA_2M_1 and PA_1M_2. It should be noticed that in the case of PA_1M_4, the signal at 165 ppm is probably the superimposition of C2 in PA_1M_4 and carbons of melamine expected around 167 and 169 ppm[17] (but difficult to observe by CP MAS since the nitrogens of the cycle bonded to the carbons are not protonated).

Scanning electron microscopy (SEM, Fig. S5) shows smooth surfaces, a typical feature for highly crystalline molecular complexes. Inductively-coupled plasma optical emission spectroscopy (ICP-OES) and elemental analysis (EA) of the crystalline materials (Fig. S3f and Table S3) reveal that the starting monomers' relative content is fully reflected in the final crystals thanks to the formation of different crystalline structures from the different monomer ratios, allowing a precise control over the elemental composition. The latter, together with the single-crystal character of the materials, illustrates the possibility enabled by this approach to tailor the design of the precursor crystalline material with excellent control over their monomers composition and organization.

In order to evaluate the potential use of the different phosphoric acid–melamine (PA_xM_y) materials as precursors of phosphorus-nitrogen-carbon materials with different elemental compositions, we studied their reaction progress by thermal gravimetric analysis (TGA) under nitrogen atmosphere (Fig. 2),

for which PA_1M_1 and PA_1M_2 were selected. The strong interactions between phosphoric acid and melamine are made evident by the significant quenching of the melamine sublimation and degradation. While melamine alone degraded completely upon heating to 800 °C, the calcination of PA_1M_1 and PA_1M_2 at 800 °C resulted in mass yields of 30 % and 17 %, respectively. Moreover, the TGA profiles reveal a close relationship between the starting sequence and the reaction progress. In the case of PA_1M_1, melamine mainly reacts with phosphoric acid and the typical condensation at ~340 °C was barely detected.[18] The increase in melamine content, which results in two melamines being in contact with each other (Fig. S1), alters the solid-state reaction course and the typical condensation is clearly prominent on the TGA profile of PA_1M_4. Therefore, phosphorus-nitrogen-carbon materials (PNC_x, where *x* is the molar ratio PA:M) with different elemental compositions were obtained by the thermal treatment of the various monocrystalline materials at 550 and 800 °C for 4 h under an inert N_2 atmosphere (see schematic in Fig. S6).

FTIR measurements of PNC_x 550 (Fig. S7a) show that the tri-*s*-triazine units' breathing mode, located at 810 cm^{-1}, gradually disappeared with increased *x* values, which illustrates how the addition of PA in the synthesis strongly modifies the typical C-N heterocycle structure of carbon-nitrogen materials prepared by thermal treatment of melamine.[19] The FTIR spectra of PNC_x synthesized at 800 °C (Fig. S7b) display four broad peaks. The peak at 750 cm^{-1}, which stems from C-O-P vibrations,[20] vanishes in the PNC_2 800 spectrum, probably due to very low carbon content in this sample. Nevertheless, stretching vibrations corresponding to phosphate groups, ν(P-O-P/ PO_4^{-3}), can be observed at 926 cm^{-1}, along with a peak at 1240 cm^{-1} which stems from a P=O stretching vibration.[21,22] At higher wavenumbers, only the stretching modes of C-N units, ν(C-N=C) can be observed at 2160 cm^{-1}. The XRD patterns of PNCs confirm that the crystal structures stray from the typical structure of heptazine-based C-N materials. $PNC_{0.25}$ 550 (Fig. S7c) exhibits the typical peaks of layered carbon nitride materials at 13.1° and 27.2°, which are usually ascribed to <100> and <002> planes, respectively.[18] The further insertion of phosphorus results in broader diffraction peaks at 25.8° for $PNC_{0.5}$ 550 and 22.6° for both PNC_1 550 and PNC_2 550, standing for a larger inter-layer spacing (*d*) which is associated with <002>. The materials prepared at 800 °C (Fig. S7d) show only a single diffraction at 22.7° for PNC_2, which shifts to higher 2ϑ values when lowering the phosphorus amount, indicating a closer packing of the layered units. Furthermore, the materials with low P content show a broader diffraction peak suggesting a more amorphous nature.

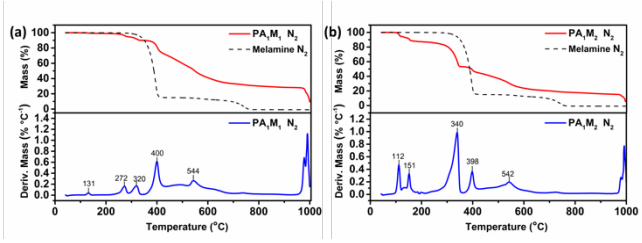

Fig. 2 Thermal gravimetric analysis (TGA) and respective derivative curves of (a) PA_1M_1 and (b) PA_1M_2 under N_2 atmosphere. The black dashed line represents pristine melamine.

X-ray photoelectron spectroscopy (XPS) analysis was carried out in order to characterize the new chemical bonds formed during the thermal condensation. Both PNC_x 550 and PNC_x 800 chemical compositions include P, C, N, and O, confirming the phosphorus preservation from the single-crystalline precursors to the final materials (Fig. S8). In the XPS P2p spectra of PNC_x 550, two species are shown at binding energies of 133.7 and 135.3 eV, standing for both P-N/ P=N bonds and oxidized phosphorus, respectively.[23–25] The N1s spectra show four species for all PNC_x 550 samples. These peaks are centered at 397.05–397.59, 398.21–398.65, 399.1–399.58, and 400.36–400.88 eV and can be assigned to both -N=P /-N-P species, C-N=C coordination, remaining amine groups, and to nitrogen oxide, respectively.[25–29] Changing the initial phosphorus amount in the precursor crystal has a significant influence on the final composition: a drop in phosphanimine species from 32 wt. % for PNC_2 550 to 5 wt. % $PNC_{0.25}$ 550, was observed. The PNC_x 550 C1s spectra (Fig. S8c) show four peaks at 284.8, 286.0, 287.8, and 290.1 eV, that correspond to the chemical states of C-C, C-O, C=N-C, and O=C-O, respectively.[30–33] A higher number of melamine units in the starting crystals resulted in a higher contribution of C-N=C, due to the formation of graphitic carbon nitride-like polymers. The XPS P2p spectra of all PNC_x 800 samples show negligible differences between the chemical states compared to PNC_x 550 (Fig. S9a). In the case of PNC_2 800, the peak corresponding to phosphanimine groups is slightly shifted to higher binding energies, probably a result of a higher oxygen content in the sample. The N1s spectra of PNC_x 800 (Fig. S9b) also show similarities to those of PNC_x 550; nevertheless, in the case of PNC_1 800 and PNC_2 800, several differences can be observed, such as an additional peak located at 401.5 eV, corresponding to the positively charged amine group, and the presence of only three nitrogen species in PNC_2 800 (full discussion and peaks assignments are given in the SI). In the case of C1s, we can conclude that the binding energies and chemical species of PNC_x 550 are partially retained in PNC_x 800 (Fig. S9c). The presence of all the above-mentioned oxides is confirmed in the O1s spectra of PNC_x 550 and PNC_x 800 (Fig. S8d and S9d).

Solid-state NMR measurements were recorded to gain additional insights about the structures of the final materials and elucidate a feasible reaction pathway. Therefore, two intermediates were synthetized at 350 and 650 °C and analyzed. ^{31}P NMR signal of PA_1M_2 single crystals shifts to more negative values upon calcination at 350 and 550 °C (Fig. 3a), suggesting the formation of P-N bonds in the structure.[6] This trend can be observed for the ^{31}P NMR spectra of the other PNC_x materials as well (Fig. S10). Additionally, upon increasing the P content and the calcination temperatures (550–800 °C), broader peaks related with the amorphous nature of the materials are observed, suggesting the existence of large distribution of phosphorus species in the structures. Considering the lack of NMR data in the literature for PN_xO_{4-x} groups, we applied structural modeling (Fig. 3c and Fig. S11) to calculate the

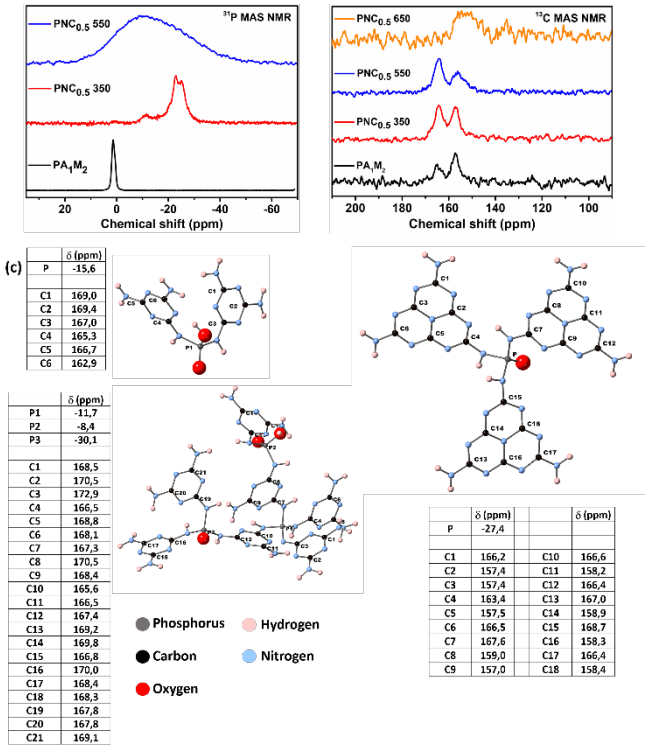

	δ (ppm)
P	-15,6
C1	169,0
C2	169,4
C3	167,0
C4	165,3
C5	166,7
C6	162,9

	δ (ppm)
P1	-11,7
P2	-8,4
P3	-30,1
C1	168,5
C2	170,5
C3	172,9
C4	166,5
C5	168,8
C6	168,1
C7	167,3
C8	170,5
C9	168,4
C10	165,6
C11	166,5
C12	167,4
C13	169,2
C14	169,8
C15	166,8
C16	170,0
C17	168,4
C18	168,3
C19	167,8
C20	167,8
C21	169,1

	δ (ppm)		δ (ppm)
P	-27,4		
C1	166,2	C10	166,6
C2	157,4	C11	158,2
C3	157,4	C12	166,4
C4	163,4	C13	167,0
C5	157,5	C14	158,9
C6	166,5	C15	168,7
C7	167,6	C16	158,3
C8	159,0	C17	166,4
C9	157,0	C18	158,4

Fig. 3 (a) ^{31}P MAS NMR spectra of PA_1M_2 raw crystal, $PNC_{0.5}$ 350, and $PNC_{0.5}$ 550. (b) ^{13}C CP MAS NMR spectra of PA_1M_2 raw crystals, $PNC_{0.5}$ 350, $PNC_{0.5}$ 550, and $PNC_{0.5}$ 650. (c) Illustration models of different phosphorus environments and their corresponding phosphorus and carbon chemical shifts.

possible ^{31}P and ^{13}C chemical shift values in different small systems in which phosphorus is coordinated to melamine or melem (2,5,8-triamino-tri-*s*-triazine) groups through P-N bonds, corresponding the different type of phosphorus environments that could be expected in these systems. The calculated ^{31}P chemical shift values are in the range from -2 to -30 ppm (Fig. 3c and Fig. S11), confirming that the large signals observed after heat-treatment are due to a distribution of PN_xO_{4-x} environments.

^{13}C CP MAS NMR spectra show two main carbon species centered around 158 and 165 ppm up to 550 °C (Fig. 3b and Fig. S12) which is not properly reproduced with the models obtained with melamine substituents of P. Indeed in this case, all carbon chemical shift values are calculated above 166 ppm consistently with melamine spectrum.[17] On the other hand, when P is linked to melem groups, two main type of chemical shifts are calculated: around 166 ppm for C linked to NH_2 groups and around 158 ppm for the other carbon atoms. This is in much better agreement with experimental data suggesting condensation of melamine into larger cyclic structures at higher temperatures.

Further analysis of the chemical composition of PNC_x materials was obtained by elemental analysis (EA) and ICP (Tables S4 and S5), which show a fine control over the elemental composition at both calcination temperatures, as well as a sheer rise in phosphorus content with higher PA-M ratios (reaching 35 wt. % for PNC_2 550 and 51 wt. % for PNC_2 800), which goes along with a strong decrease in the relative nitrogen and carbon content. Moreover, the disappearance of one of the carbon species,

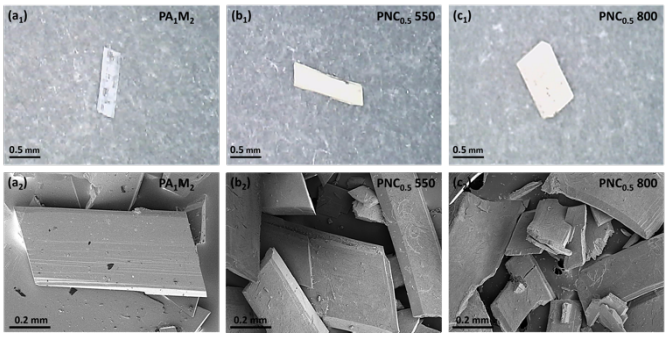

Fig. 4 Optical (top row) and SEM (bottom row) images of (a) a PA_1M_2 raw single crystal and its corresponding products after calcination at (b) 550 °C and (c) 800 °C.

which is evident from the $PNC_{0.5}$ 650 NMR ^{13}C spectrum and is likely caused by a partial oxidation, is also well-supported by the EA results since the carbon content dramatically drops at calcination temperatures above 550 °C. It is important to emphasize that it is typical to observe a decrease of nitrogen during the formation of carbon nitride materials; however, here, because the P-N bond is strong compared to the C-N bond, the nitrogen is better retained upon heating and the relative amount of carbon is decreased.

The control over the final composition of the materials leads to tunable absorption features as seen in Fig. S13, which in turn permit their potential uses as light-harvesting materials. The morphology of the PNC_x materials, studied by SEM, strongly depends on the chemical composition and calcination temperature. The morphologies of PNC_x 550 (Fig. S14) span the typical unordered features of melamine-based carbon nitrides in case of $PNC_{0.25}$ 550 to a more homogeneous and smoother morphology and structure at higher phosphorous content, reaching a large 2D sheets morphology for PNC_2 550. Notably, even upon calcination at 800 °C, the size and shape of the molecular single crystals was completely preserved (Fig. 4). The preservation of the shape and chemical composition accentuates the uniqueness and versatility of utilizing organic single crystals for the design of functional carbon materials with targeted heteroatom insertion. For the PNC_x 800, more ordered structures with smoother surfaces were observed upon increasing phosphorous content (Fig. 5a–d). Transmission electron microscope (TEM, Fig. 5e–h) images reveal a layered structure for all PNC_x 800. The PNC_2 800 is composed of very large (>2 µm), continuous and smooth 2D sheet-like morphology, while at lower *x* value, the layer's size decreases, and a more porous structure is observed. Importantly, energy-filtered TEM (EFTEM) for all PNC_x 800 (Fig. 5i–l and Fig. S15) shows a homogenous distribution of phosphorus, nitrogen, carbon, and oxygen within the material.

Having all the data in hand, we can conclude that the starting monomers sequence in the starting crystal strongly guides the reaction path as well as the growth and final properties of the materials after calcination at high temperature (Fig. 2a). The high degree of order in the starting crystals together with the strong hydrogen bond interactions keep the PA and M molecules in the same starting position even at high temperatures, leading to the reaction of adjacent molecules according to the placement in the starting crystal. The

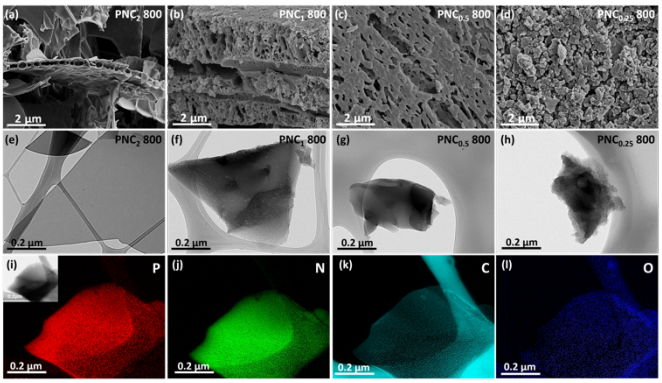

Fig. 6 Electron microscopy characterization of PNC_x synthesized at 800 °C, *x* standing for the precursors' molar ratio (PA:M). SEM images of *x* = (a) 2, (b) 1, (c) 0.5, and (d) 0.25. TEM images of *x* = (e) 2, (f) 1, (g) 0.5, and (h) 0.25. EFTEM images of PNC_1 800: (i) phosphorus marked in red (inset image of the attributed PNC_1 800), (j) nitrogen marked in green, (k) carbon marked in cyan, and (l) oxygen marked in blue.

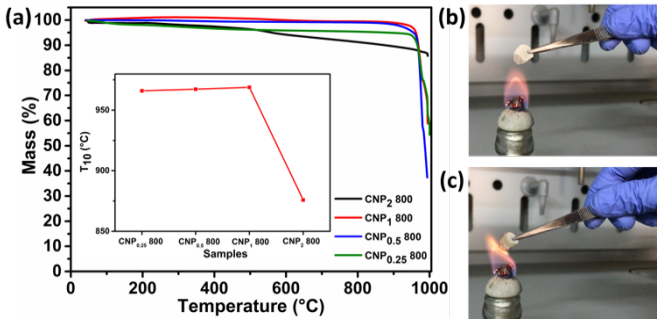

Fig. 5 (a) TGA measurements under air of all PNC prepared at 800 °C. Inset graph shows the corresponding T_{10} values of PNC_x 800 (the temperature at which 10% of the mass is lost). (b) and (c) Optical photographs of PNC_1 800 soaked with alcohol, during the burning with an ethanol lamp (see also movie-1).

monomers sequence determines the materials' type that will be synthesized in a great accuracy, endowing the final products with a great versatility in their electronic, optical, and other properties as will be discussed below.

The excellent preservation of the single-crystal precursors macrostructure, *i.e.* shape and size, presents a unique opportunity to directly measure the electrical properties of the $PNC_{0.5}$ materials by a single conductivity measurement (Fig. S16). For this analysis, $PNC_{0.5}$ at 550 and 800 °C were selected and the recorded conductivity values were compared to state-of-the-art values for CN materials measured using the same technique. $PNC_{0.5}$ 550 showed a higher conductivity value than $PNC_{0.5}$ 800, probably a consequence of a higher carbon content within $PNC_{0.5}$ 550 than in $PNC_{0.5}$ 800 (Fig. S16b). Interestingly, the conductivity of both $PNC_{0.5}$ materials is two orders of magnitude higher than that of the reported needle-shaped carbon nitride synthesized at 500 °C, which confirm a higher degree of delocalized free electrons in the $PNC_{0.5}$ samples and the lack of crystals boundaries.[12]

TGA measurements under air were used to evaluate the stability of the new materials to oxidation and their suitability as fire-retardant materials. PNC_x 550 TGA curves (Fig. S17) confirm the good stability of these materials, especially for PNC_2 550 and PNC_1 550 due to a larger number of P=N bonds. TGA analysis of the final PNC_x 800 materials (Fig. 6a) demonstrates their remarkable stability, with up to 90% of the starting mass retained at 970 °C, as shown by the T_{10} values (the temperatures at which 10% of the material's mass is lost, Fig. 6a inset plot). The thermal stability of PNC_x was further analyzed by exposing them to an open flame. PNC_1 800 was burnt over an ethanol lamp flame (Fig. 6b–c, and SI movie). The mass of the sample after burning was about two times higher than before burning due to additional oxygen, confirming its high stability compared to P-doped carbon-nitrogen materials. XPS of PNC_1 800 after burning (Fig. S18) shows that two oxide species have been formed including carbonyl and hydroxyl groups, and the peaks corresponding to the C-N=C group in both N1s and C1s spectra completely vanished, suggesting some carbon release. The high thermal stability, owing to the P-N bonds, together with the high degree of composition tunability, opens the opportunity to utilize the PNC_x materials as halogen-free fire-retardant materials, support for high temperature catalysis, metal-air batteries and other applications which require high-temperature stability.

To demonstrate the high thermal stability of PNC_x 800, we introduced them as a lightweight metal-free support for Ni catalysts in a catalytic reaction at high temperature. With this purpose, CO_2 methanation (Sabatier reaction) was selected as model reaction. This is typically conducted in the industry at high temperatures (ca. 400 °C) by means of metallic catalysts (Ni, Ru, etc.) supported on metal oxides (Al_2O_3, TiO_2, ZrO_2, CeO_2). Ni/PNC_x 800 catalysts were synthesized by wet impregnation of 25 wt. % Ni^{II} nitrate salt on PNC_x 800 followed by thermal reduction under H_2 atmosphere (see SI for further details). XRD patterns of all Ni/PNC_x 800 materials (Fig. 7a) confirm the formation of the metallic nickel alongside the amorphous PNC_x 800 (which is responsible for the diffraction ca. 22.7°). These measurements also show some negligible peaks corresponding to NiO. It is worth noticing that under reaction conditions (2.0 bar H_2, 0.5 bar CO_2 and *T* = 400 °C) NiO species should be reduced to Ni^0. Some representative HRTEM images of Ni/PNC_2 800 are presented in Fig. S19. Round small nanoparticles (NPs) of different sizes are homogeneously distributed over the PNC surface. Energy dispersive X-ray spectroscopy (EDS) analysis confirmed Ni as the main element of the observed NPs. In all cases, a wide size distribution, ranging from few nanometers to about 100 nm is measured, with an average particle size of 35±19 nm.

The catalytic activity of three different Ni/PNC_x 800 materials was examined for CO_2 methanation at 400 °C. 20 mg of Ni/PNC_x 800 catalyst were placed in a cylindrical reactor (51 mL) equipped with a thermocouple connected to an electrical heating ribbon and temperature controller. H_2 and CO_2 gases were loaded at partial pressures of 2.0 and 0.5 bar, respectively (see additional details in ESI). All Ni/PNC_x 800 samples showed CH_4 production after a reaction time of 20 h (Fig. 7b), and other gases as CO were not detected. It is also worth commenting that in the absence of Ni NPs, the PNC_x 800 materials do not show catalytic activity at these conditions, confirming the role of the Ni metal as the active catalyst in this reaction. CH_4 production has been normalized by the Ni mass measured using ICP-OES (Fig. S20). Fig. 7a shows that the three different Ni/PNC_x 800

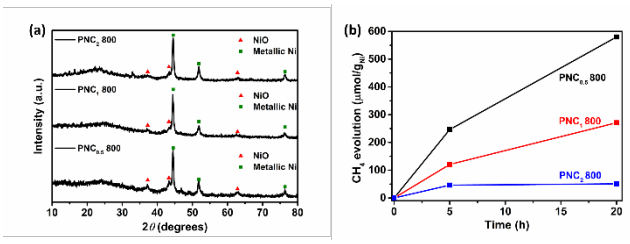

Fig. 7 (a) XRD patterns: green squares – metallic nickel (*fcc* Ni) PDF 00-004-0850 (ICDD, 2002); red triangles– NiO PDF 00-044-1159 (ICDD, 2002). (b) CH_4 evolution from the different Ni/PNC_x 800 catalysts at 400 °C. Reaction conditions: $P(H_2)$ = 2.5 bar; $P(CO_2)$ = 0.5 bar. Catalysts: m = 20 mg.

catalysts produced different CH_4 amounts after 20 h. This indicates that the PNC_x 800 substrates act not only as support for the Ni catalyst, but also there is a strong interaction between the supports and the Ni NPs. Thus, fine-tuning the PNC composition gives rise to an enhancement of the Ni catalytic activity, probably due to the different nitrogen content present in these samples, which have been reported to strongly interact with Ni NPs, enhancing their reactivity.[34,35]

Besides the differences in CH_4 evolution observed from the different catalysts, which is beyond the scope of this work, we were more interested investigating their thermal stability in high-temperature reactions. Fig. 7b shows that all catalysts suffered deactivation after long reaction times (20 h), although Ni/PCN_2 800 suffered higher deactivation than the other two samples.

HRTEM images of the catalysts after 20 h reaction at 400 °C (Fig. S21) show that the PNC_x supports did not suffer apparent structural changes under the experimental CO_2 methanation reaction conditions. However, large Ni aggregates were formed, especially in the case of PNC_2. Deconvolution of XPS spectra to their individual components was also performed to investigate the PNC_2 800 stability (Fig. S22). The C1s spectrum of $PNC_{0.5}$ 800 did not undergo significant changes during the reaction. P1s and N1s spectra present an enhancement in P and N oxide species, and the component attributed to H_2O in the O1s spectrum increased notably after reaction. The rise of adsorbed water and oxidized species is not surprising since water is the byproduct in the Sabatier reaction. Overall, the aggregation of the Ni NPs has been identified as the main deactivation mechanism, although water adsorption could also influence the CH_4 production. This behavior has been previously reported for Ni-supported carbon-based catalysts and we believe it to be the most probable deactivation mechanism.[36]

Conclusions

We demonstrated here a general and simple method to precisely control the elemental ratio, morphology, and properties (structural, electronic, and thermal) of phosphorus-nitrogen-carbon materials, spanning polyphosphazenes, carbon-nitrogen-phosphorous materials, and P-doped carbon nitride, by utilizing tailored organic single crystals as precursors in a high temperature solid-state reaction. To do so, we designed four different supramolecular crystal melamine-phosphate structure with different crystal structures and elemental compositions. Detailed structural analysis together with solid-state NMR modeling reveal that upon calcination, the starting order of the molecules within the single crystals directs the reaction path as well as determines the final materials' composition and properties. We demonstrated that fine-tuning the final materials' composition permits the control over their optical and electrical properties, as well as over their stability to oxidation at high temperature. Consequently, the materials exhibit a remarkable resistance to thermal oxidation, retaining up to 90% of the starting material at 970 °C in air. We exemplified the exploitation of the new materials as a stable substrate in a catalytic reaction at high temperature (400 °C), specifically, CO_2 methanation. Moreover, the catalytic activity can be altered by the elemental composition of the substrate, owing to the substrate–catalyst interaction of Ni/PNC_x. We believe that the presented design approach based on using single crystals with pre-designed monomers sequence as the precursors is a significant step towards the formation of materials with highly addressable composition and properties. This will be used to guide the synthesis of new materials with great control over their atomic composition, electrical, and structural properties as well as thermal stability to oxidation, enabling their exploitation in fire retardant, electrochemical, and catalytic applications.

Experimental

Materials

Orthophosphoric acid (H_3PO_4 85 wt. %, Bio-Lab Chemicals), Melamine (99 %, Alfa Aesar), 2-propanol (LOBA Chemie), nickel (II) nitrate hexahydrate ($Ni(NO_3)_2{\cdot}6H_2O$, 97%, Sigma-Aldrich), nitric acid (HNO_3 67–69 wt. %, trace metal grade, Fisher Chemical) and acetone (Bio-Lab AR grade) were used without additional purification. Deionized (DI) water were purified using a Millipore Direct-Q3 UV to a Type I grade (18.2 MΩ cm resistivity) and was used as the solvent in all experiments.

Synthetic procedures

Phosphorus-nitrogen-carbon composite synthesis

First, phosphoric acid-melamine single crystals were prepared by dissolving 1.0 g of melamine in 150 mL of deionized (DI) water, different amounts of phosphoric acid (85 wt. % in H_2O) were then added to the melamine solution in order to reach molar ratios of 2:1, 1:1, 1:2, 1:4 (H_3PO_4:melamine). After complete dissolution, the solvent was slowly evaporated at room temperature and parallelogram-shaped crystals were obtained after ~2.5 weeks, with 90–93% yields. Synthesis of PNC materials was carried out by a thermal treatment of the prepared single-crystals under inert N_2 atmosphere at 550 and 800 °C for 4 h using a constant heating ramp rate of 1.96 and 3.0 °C min^{-1}, respectively.

Nickel deposition on PNC_x 800

Ni-PNC_x 800 (x = 2, 1, 0.5) were prepared by using a wet impregnation technique. First, an aqueous solution of $Ni(NO_3)_2{\cdot}6H_2O$ were obtained by dissolving 25 wt. % of Ni(II) in DI water; the solution was then added dropwise to each

aqueous PNC_x 800 dispersion. The resulting Ni(II)-PNC_x 800 were filtered and dried overnight at 70 °C. Ni(II) was reduced to its metallic state under hydrogen flow (flow rate of 100 mL min^{-1}) at 350 °C for 3 h using a constant heating ramp rate of 10 °C min^{-1}. The resulting Ni-PNC_x 800 materials were washed with acetone and water to remove unreacted metallic salts and dried overnight.

Characterizations

Powder X-ray diffraction (P-XRD) patterns were performed by using a PANalytical Empyrean diffractometer. Elemental analysis (EA) data for CHNO were collected by using a Thermo Scientific Flash Smart elemental analyzer OEA 2000. Phosphorus content was determined by dissolving the samples in concentrated nitric acid in a PTFE-lined autoclave for 8 h at 180 °C, and analyzing the sample using a Spectro ARCOS ICP-OES, FHX22 Multi View Plasma instrument. High resolution transmission electron microscopy (HRTEM) were performed on a JEOL JEM-2100F analytical instrument operated at U_0 = 200 kV with energy-filtered TEM (EFTEM) analysis obtained using a Gatan image filter. For EFTEM, P-L (132 eV), N-K (400 eV), C-K (284 eV), and O-K (532 eV) edges were recorded by using three-window method. FTIR spectra were acquired on a Thermo Scientific Nicolet 6700 spectrometer in the 650–4000 cm^{-1} range. UV-vis spectra were measured by using a Cary 100 spectrophotometer equipped with a DRA (integrating sphere), in reflectance mode. Photoluminescence measurements were collected by using Fluorolog TCSPC HORIBA Scientific spectrofluorimeter with an excitation wavelength λ_{ex} = 360 nm. XPS spectra were collected by using ESCALAB 250 ultrahigh vacuum (1×10^{-9} bar) apparatus with an Al-Kα X-ray source and a monochromator. The X-ray beam size was 500 µm and survey spectra was recorded with a pass energy (PE) of 150 eV and high energy resolution spectra were recorded with a PE of 20 eV an X-ray photoelectron spectrometer. All XPS spectra were calibrated relative to the C 1s peak, positioned at 284.6 eV. The XPS results were processed by using the AVANTAGE software. Thermal gravimetric analyses were carried on thermal gravimetric analyzer Q500 model under inert N_2 environment and under air for the PNC precursors and PNC final materials, respectively. SEM images were obtained using an FEI Verios 460Lhigh-resolution SEM, equipped with a FEG source, and operated at U_0 = 3.0 kV. Single crystal X-ray diffraction (SC-XRD) measurements were acquired in order to elucidate the exact structures of the PNC precursors. SC-XRD analysis of PA_2M_1, PA_1M_2, PA_1M_4, were carried out on a Bruker kappa APEXII Diffractometer. A single crystal measurement of PA_1M_1 was performed on a XtaLAB Synergy, Dualflex, HyPix diffractometer. Using Olex2,[37] the structure was solved with the ShelXT[38] structure solution program using Intrinsic Phasing and refined with the ShelXL[39] refinement package using least squares minimization. The crystal was kept at 293(2) K during data collection.

Solid-state ^{13}C CP MAS NMR spectra were recorded on a Bruker AVANCE 300 spectrometer (7.0 T, $\nu_0(^1H)$ = 300.29 MHz, $\nu_0(^{13}C)$ = 75.51 MHz) using a 4 mm Bruker probe and a spinning frequency of 10 kHz. ^{31}P MAS NMR spectra were recorded on a Bruker AVANCE III 700 spectrometer (16.3 T, $\nu_0(^{31}P)$ = 283.54 MHz) using a 2.5 mm Bruker probe spinning at 20 kHz and on a Bruker AVANCE 300 spectrometer (7.0 T, $\nu_0(^1H)$ = 300.29 MHz, $\nu_0(^{31}P)$ = 75.51 MHz) using a 4 mm Bruker probe and a spinning frequency of 12.5 kHz. ^{13}C CP MAS experiments were recorded with ramped-amplitude cross-polarization in the ^1H channel to transfer magnetization from ^1H to ^{13}C. (Recycle delay = 3s, CP contact time = 1 ms, optimized ^1H spinal-64 decoupling). Single pulse ^{31}P MAS NMR spectra were recorded with a recycle delay of 10 to 40 s depending on the samples.

Chemical shift values were referenced to tetramethylsilane (TMS) for ^{13}C and H_3PO_4 (85 wt. %) for ^{31}P.

Structural models, including crystalline structures, were relaxed with the VASP (Vienna Ab-initio Simulation Package) code[40] based on the Kohn-Sham Density Functional Theory (DFT) and using a plane-wave pseudopotential approach. The integral over the first Brillouin zone are performed using a Monkhorst-Pack 1×1×1 k-point grid[41] The electron-ion interaction was described by the projector augmented-wave (PAW) method[42] with a 300 eV energy cutoff.

The NMR parameters were calculated within Kohn-Sham DFT using the QUANTUM-ESPRESSO code,[43,44] keeping the atomic positions equal to the values previously calculated with VASP. The PBE generalized gradient approximation[45] was used and the valence electrons were described by norm conserving pseudopotentials[46] in the Kleinman Bylander form.[47] The shielding tensor was computed using the Gauge Including Projector Augmented Wave (GIPAW) approach,[48] which enables the reproduction of the results of a fully converged all electron calculation.[49] Absolute shielding tensors were obtained. To set the ^{31}P and ^{13}C chemical shift scale, the calculated δ_{iso} for reference compounds were compared to experimental values so that the average sum of experimental and calculated shifts coincide, as previously described.[6]

Conductivity measurements of the $PNC_{0.5}$ synthesized at 550, 650, and 800 °C were performed by the two contacts method. The $PNC_{0.5}$ was contacted using a graphite ink between two Tungsten tips and a voltage bias between −10 V and +10 V was applied at room temperature. Electric current values are recorded and an I–V curve is obtained, to allow the physical parameters calculation of the PNC parallelogram-shaped using Ohm's Law (V = IR), where I (A) is the current and R (Ω) is the resistance; since the resistance depends on the geometric parameters of the sample, the value is expressed as resistivity, ρ = R(S/L), where S is the transversal section area of the sample and L is the distance between the two contact points. To calculate the thickness (E) of $PNC_{0.5}$, scanning electron microscopy (SEM) was used. Conductivity measurements [$\sigma = \rho^{-1}$ (S cm^{-1})] were performed by measuring three parallelogram-shaped crystals of the same sample and obtaining an average value.

CO_2 methanation was conducted in a 51 mL quart reactor equipped with a nickel alloy thermocouple combined with a heating mantle and temperature controller. H_2 and CO_2 gases were loaded in stoichiometric amounts of 5:1. The initial reaction time (t = 0) corresponds to a reactor temperature of 400 °C, after equilibration, which typically takes 30 min. CH_4

evolution was analyzed by measuring the gases formed during the gas-phase reaction with an Agilent 490 MicroGC. The values of CO_2 conversion were quantified based on prior calibration of the system injecting mixtures with known percentage of gases.

Conflicts of interest

There are no conflicts to declare.

Acknowledgements

The authors would like to thank Dr. Volodiya Ezersky, Dr. Natalya Froumin, Dr. Anna Milionshchik, Dr. Radion Vainer, Dr. Einat Nativ-Roth, and Mr. Nitzan Shauloff for analytical HRTEM, XPS, TGA, SC-XRD, HRSEM, and technical support, respectively. This research was partly funded by the following: the Planning & Budgeting Committee/Israel Council for Higher Education (CHE) and Fuel Choice Initiative (Prime Minister Office of Israel), within the framework of "Israel National Research Center for Electrochemical Propulsion" (INREP); the Minerva Center No. 117873; the Spanish Ministerio de Economía y Competitividad (MAT2016-77608-C3-1-P, MAT2016-75883-C2-2-P); J. A and H. G. also gratefully acknowledges financial support from the Spanish Ministry of Economy and Competitiveness (Severo Ochoa SEV2016-0683 and RTI2018-89023-CO2-R1) and by the Generalitat Valenciana (Prometeo 2017–083). This project has received funding from the European Research Council (ERC) under the European Union's Horizon 2020 research and innovation programme (grant agreement No. [849068]). NMR spectroscopic calculations were performed using HPC resources from GENCI-IDRIS (Grant 097535). The French Region Ile de France-SESAME program is acknowledged for financial support (700 MHz spectrometer).

Notes and References

1 D. S. Su, J. Zhang, B. Frank, A. Thomas, X. Wang, J. Paraknowitsch and R. Schlögl, *ChemSusChem*, 2010, **3**, 169–180.

2 J. P. Paraknowitsch and A. Thomas, *Energy Environ. Sci.*, 2013, **6**, 2839–2855.

3 D. P. Gates, *Angew. Chemie Int. Ed.*, 2003, **42**, 4570–4570.

4 E. Cruz-Silva, D. A. Cullen, L. Gu, J. M. Romo-Herrera, E. Muñoz-Sandoval, F. López-Urías, B. G. Sumpter, V. Meunier, J. Charlier, D. J. Smith, H. Terrones and M. Terrones, *ACS Nano*, 2008, **2**, 441–448.

5 E. Cruz-Silva, F. López-Urías, E. Muñoz-Sandoval, B. G. Sumpter, H. Terrones, J. Charlier, V. Meunier and M. Terrones, *ACS Nano*, 2009, **3**, 1913–1921.

6 W. Zhang, J. Barrio, C. Gervais, A. Kocjan, A. Yu, X. Wang and M. Shalom, *Angew. Chemie Int. Ed.*, 2018, **57**, 9764–9769.

7 M. M. Velencoso, A. Battig, J. C. Markwart, B. Schartel and F. R. Wurm, *Angew. Chemie - Int. Ed.*, 2018, **57**, 10450–10467.

8 C. Li, Z. Chen, A. Kong, Y. Ni, F. Kong and Y. Shan, *J. Mater. Chem. A*, 2018, **6**, 4145–4151.

9 A. B. Chaplin, J. A. Harrison and P. J. Dyson, *Inorg. Chem.*, 2005, **44**, 8407–8417.

10 S. Guo, Z. Deng, M. Li, B. Jiang, C. Tian, Q. Pan and H. Fu, *Angew. Chemie - Int. Ed.*, 2016, **55**, 1830–1834.

11 L. L. Feng, Y. Zou, C. Li, S. Gao, L. J. Zhou, Q. Sun, M. Fan, H. Wang, D. Wang, G. D. Li and X. Zou, *Int. J. Hydrogen Energy*, 2014, **39**, 15373–15379.

12 J. Barrio, L. Lin, P. Amo-Ochoa, J. Tzadikov, G. Peng, J. Sun, F. Zamora, X. Wang and M. Shalom, *Small*, 2018, **14**, 1800633.

13 C. F. J. Faul and M. Antonietti, *Adv. Mater.*, 2003, **15**, 673–683.

14 J. Barrio and M. Shalom, *ChemCatChem*, 2018, **10**, 5573–5586.

15 D. J. A. De Ridder, K. Goubitz, V. Brodski, R. Peschar and H. Schenk, *Helv. Chim. Acta*, 2004, **87**, 1894–1905.

16 X. Li, S. Feng, F. Wang, Q. Ma and M.-L. Zhu, *Acta Crystallogr. Sect. E Struct. Reports Online*, 2010, **66**, o239–o240.

17 B. Jürgens, E. Irran, J. Senker, P. Kroll, H. Müller and W. Schnick, *J. Am. Chem. Soc.*, 2003, **125**, 10288–10300.

18 J. Barrio, A. Grafmüller, J. Tzadikov and M. Shalom, *Appl. Catal. B Environ.*, 2018, **237**, 681–688.

19 Y. C. Zhao, D. L. Yu, H. W. Zhou, Y. J. Tian and O. Yanagisawa, *J. Mater. Sci.*, 2005, **40**, 2645–2647.

20 A. D. Naik, G. Fontaine, F. Samyn, X. Delva, J. Louisy, S. Bellayer, Y. Bourgeois and S. Bourbigot, *Fire Saf. J.*, 2014, **70**, 46–60.

21 I. Němec, Z. Macháčková, K. Teubner, I. Císařová, P. Vaněk and Z. Mička, *J. Solid State Chem.*, 2004, **177**, 4655–4664.

22 P. Lv, Z. Wang, K. Hu and W. Fan, *Polym. Degrad. Stab.*, 2005, **90**, 523–534.

23 P. Zhu, Z. Yang, H. Zhang, J. Yu, Z. Zhang, J. Cai and C. Li, *J. Alloys Compd.*, 2018, **745**, 164–171.

24 M. Guo, J. Huang, X. Kong, H. Peng, H. Shui, F. Qian, L. Zhu, W. Zhu and Q. Zhang, *New Carbon Mater.*, 2016, **31**, 352–362.

25 J. Wu, S. Yang, J. Li, Y. Yang, G. Wang, X. Bu, P. He, J. Sun, J. Yang, Y. Deng, G. Ding and X. Xie, *Adv. Opt. Mater.*, 2016, **4**, 2095–2101.

26 A. Fukushima, A. Hayashi, H. Yamamura and M. Tatsumisago, *Solid State Ionics*, 2017, **304**, 85–89.

27 M. Xie, J. Tang, L. Kong, W. Lu, V. Natarajan, F. Zhu and J. Zhan, *Chem. Eng. J.*, 2019, **360**, 1213–1222.

28 J. Yue and A. J. Epstein, *Macromolecules*, 1991, **24**, 4441–4445.

29 S. Sugai, H. Watanabe, T. Kioka, H. Miki and K. Kawasaki, *Surf. Sci.*, 1991, **259**, 109–115.

30 P. Goli, S. Legedza, A. Dhar, R. Salgado, J. Renteria and A. A. Balandin, *J. Power Sources*, 2014, **248**, 37–43.

31 G. Wulff, H. Schmidt and L. Zhu, *Macromol. Chem. Phys.*, 1999, **200**, 774–782.

32 J. Xu, L. Zhang, R. Shi and Y. Zhu, *J. Mater. Chem. A*, 2013, **1**, 14766.

33 G. U. Kulkarni, S. Laruelle and M. W. Roberts, *Chem. Commun.*, 1996, 9–10.

34 L. Wang, C. Wang, X. Hu, H. Xue and H. Pang, *Chem. – An Asian J.*, 2016, **11**, 3305–3328.

35 J. Barrio, D. Mateo, J. Albero, H. García and M. Shalom, *Adv. Energy Mater.*, 2019, **9**, 1902738.

36 D. Mateo, J. Albero and H. García, *Appl. Catal. B Environ.*, 2018, **224**, 563–571.

37 O. V. Dolomanov, L. J. Bourhis, R. J. Gildea, J. A. K. Howard and H. Puschmann, *J. Appl. Crystallogr.*, 2009, **42**, 339–341.

38 G. M. Sheldrick, *Acta Crystallogr. Sect. A Found. Crystallogr.*, 2015, **71**, 3–8.

39 G. M. Sheldrick, *Acta Crystallogr. Sect. C Struct. Chem.*, 2015, **71**, 3–8.

40 G. Kresse and J. Hafner, *Phys. Rev. B*, 1994, **49**, 14251–14269.

41 J. D. Pack and H. J. Monkhorst, *Phys. Rev. B*, 1977, **16**, 1748–1749.

42 P. E. Blöchl, O. Jepsen and O. K. Andersen, *Phys. Rev. B*, 1994, **49**, 16223–16233.

43 P. Giannozzi, S. Baroni, N. Bonini, M. Calandra, R. Car, C. Cavazzoni, D. Ceresoli, G. L. Chiarotti, M. Cococcioni, I. Dabo, A. Dal Corso, S. de Gironcoli, S. Fabris, G. Fratesi, R. Gebauer, U. Gerstmann, C. Gougoussis, A. Kokalj, M. Lazzeri, L. Martin-Samos, N. Marzari, F. Mauri, R. Mazzarello, S. Paolini, A. Pasquarello, L. Paulatto, C. Sbraccia, S. Scandolo, G. Sclauzero, A. P. Seitsonen, A. Smogunov, P. Umari and R. M. Wentzcovitch, *J. Phys. Condens. Matter*, 2009, **21**, 395502.

44 S. Baroni, S. de Gironcoli, A. Dal Corso and P. Giannozzi, *Rev. Mod. Phys.*, 2001, **73**, 515–562.

45 J. P. Perdew, K. Burke and M. Ernzerhof, *Phys. Rev. Lett.*, 1996, **77**, 3865–3868.

46 N. Troullier and J. L. Martins, *Phys. Rev. B*, 1991, **43**, 1993–2006.

47 L. Kleinman and D. M. Bylander, *Phys. Rev. Lett.*, 1982, **48**, 1425–1428.

48 C. J. Pickard and F. Mauri, *Phys. Rev. B - Condens. Matter Mater. Phys.*, 2001, **63**, 2451011–2451013.

49 K. Lejaeghere, G. Bihlmayer, T. Bjorkman, P. Blaha, S. Blugel, V. Blum, D. Caliste, I. E. Castelli, S. J. Clark, A. Dal Corso, S. de Gironcoli, T. Deutsch, J. K. Dewhurst, I. Di Marco, C. Draxl, M. Du ak, O. Eriksson, J. A. Flores-Livas, K. F. Garrity, L. Genovese, P. Giannozzi, M. Giantomassi, S. Goedecker, X. Gonze, O. Granas, E. K. U. Gross, A. Gulans, F. Gygi, D. R. Hamann, P. J. Hasnip, N. A. W. Holzwarth, D. Iu an, D. B. Jochym, F. Jollet, D. Jones, G. Kresse, K. Koepernik, E. Kucukbenli, Y. O. Kvashnin, I. L. M. Locht, S. Lubeck, M. Marsman, N. Marzari, U. Nitzsche, L. Nordstrom, T. Ozaki, L. Paulatto, C. J. Pickard, W. Poelmans, M. I. J. Probert, K. Refson, M. Richter, G.-M. Rignanese, S. Saha, M. Scheffler, M. Schlipf, K. Schwarz, S. Sharma, F. Tavazza, P. Thunstrom, A. Tkatchenko, M. Torrent, D. Vanderbilt, M. J. van Setten, V. Van Speybroeck, J. M. Wills, J. R. Yates, G.-X. Zhang and S. Cottenier, *Science (80-.).*, 2016, **351**, aad3000–aad3000.

Supplementary Information for

Synthesis of Metal-Free Lightweight Materials with Sequence-Encoded Properties

Adi Azoulay[a], Jesús Barrio[a], Jonathan Tzadikov[a], Michael Volokh[a], Josep Albero[b], Christel Gervais[c], Pilar Amo-Ochoa[d], Hermenegildo García[b], Félix Zamora[d,e], Menny Shalom[a]*

a. Department of Chemistry and Ilse Katz Institute for Nanoscale Science and Technology, Ben-Gurion University of the Negev, Beer-Sheva 8410501, Israel. E-mail: mennysh@bgu.ac.il

b. Instituto Universitario Mixto de Tecnología Química (UPV-CSIC), Universitat Politècnica de València, Avda. de los Narajos s/n, 46022, Valencia, Spain.

c. Sorbonne Université, College de France, Laboratoire de Chimie de la Matière Condensée de Paris (LCMCP), UMR CNRS 7574 4 place Jussieu, 75252 Paris cedex 05, France.

d. Departamento de Química Inorgánica, Institute for Advanced Research in Chemical Sciences (IAdChem) and Condensed Matter Physics Center (IFIMAC). Universidad Autónoma de Madrid, E-28049 Madrid, Spain.

e. Instituto Madrileño de Estudios Avanzados en Nanociencia (IMDEA-Nanociencia). Cantoblanco E-28049 Madrid, Spain.

Table S1. Crystal structure parameters of bis(2,4,6-triamino-1,3,5-triazin-1-ium) hydrogen phosphate trihydrate, 2,4,6-triamino-1,3,5-triazinium orthophosphate and 2,4,6-triamino-*s*-triazine.

	PA_2M_1 [1] 2,4,6-triamino-1,3,5-triazinium orthophosphate	**PA_1M_2** [2,3] bis(2,4,6-triamino-1,3,5-triazin-1-ium) hydrogen phosphate trihydrate	**PA_1M_4** [4] 2,4,6-triamino-*s*-triazine
Temperature (K)	296	296	296
Empirical formula	$C_3H_9N_6O_4P$	$C_6H_{21}N_{12}O_7P$	$C_3H_5N_6$
Space group	*P*-1	*P*-1	$P2_1/n$
Crystal system	Triclinic	Triclinic	Monoclinic
***a* (Å)**	4.58	6.81	7.29
***b* (Å)**	9.37	10.58	7.49
***c* (Å)**	10.24	12.52	10.40
***α* (°)**	83.42	91.80	90
***β* (°)**	88.24	105.65	108.43
***γ* (°)**	85.38	108.11	90

Table S2. Single-crystal X-ray CIF data of new PA_1M_1 crystal.

	PA_1M_1
Temperature (K)	293
Empirical formula	$C_3H_{12}N_6O_8P_2$
***M* /g mol $^{-1}$**	322.13
Space group	*P2/c*
Crystal size/mm	0.1 × 0.1 × 0.1
Crystal System	Monoclinic
***a* (Å)**	4.57630(10)
***b* (Å)**	8.0571(2)
***c* (Å)**	16.5465(4)
***α* (°)**	90
***β* (°)**	95.331(2)
***γ* (°)**	90
***V* (Å^3)**	607.46(2)
Z	2
***ρ* (g cm^{-3})**	1.761
***μ* (mm^{-1})**	3.789
***F*(000)**	332.0
Ab. correct.	multi-scan
T_{min}/ T_{max}	0.719/ 0.685
$2\Theta_{max}$	136.736
Total reflns.	2147
Unique reflns.	1113
Obs. reflns.	1034
R_{int}	0.0504
Radiation	CuKα
Wavelength (Å)	1.54184
***hkl* range**	$-5 \le h \le 5$
	$-9 \le k \le 9$
	$-1 \le l \le 19$

No. of reflections	1113
No. of parameters	115
R1 [I> 2σ(I)]	0.0487
wR2 [I> 2σ(I)]	0.1273
R1[all data]	0.0505
wR2 [all data]	0.1293
Goodness of fit	1.113
$\Delta\rho_{max}$, $\Delta\rho_{min}$(eÅ^{-3})	0.51, –0.31
CCDC no.	1923238

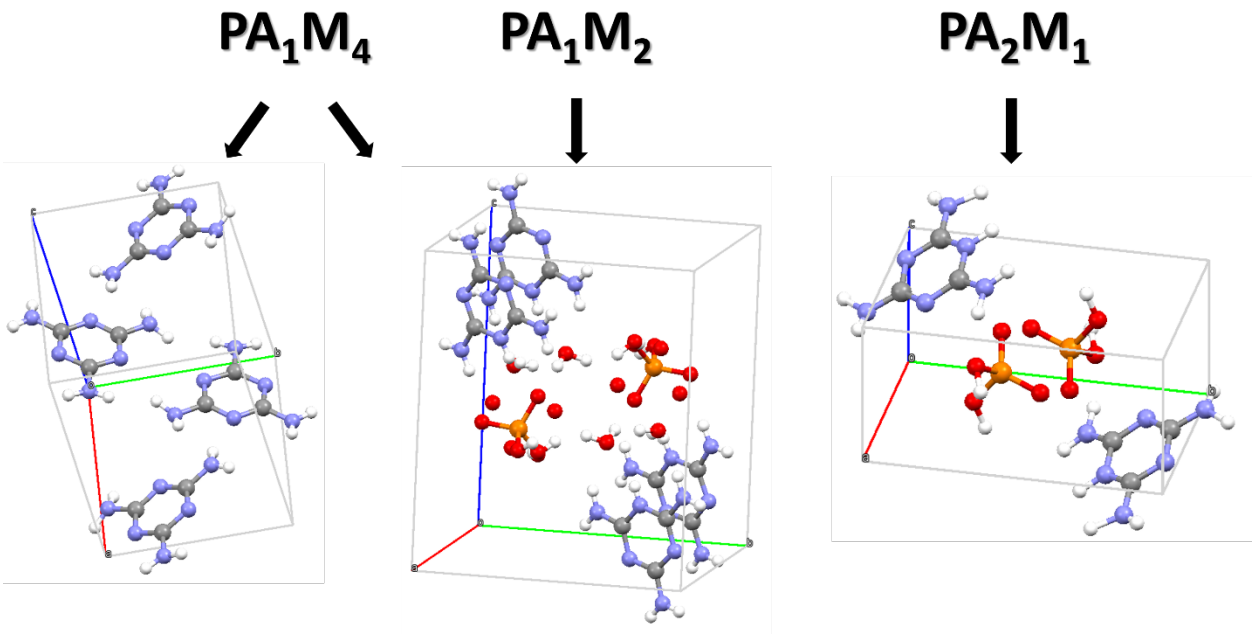

Fig. S1 PA_xM_y single crystal packing structures. In all three cells the orientation is as follows: "a" axis is marked in red, "b" axis is marked in green, and "c" axis is marked in blue.

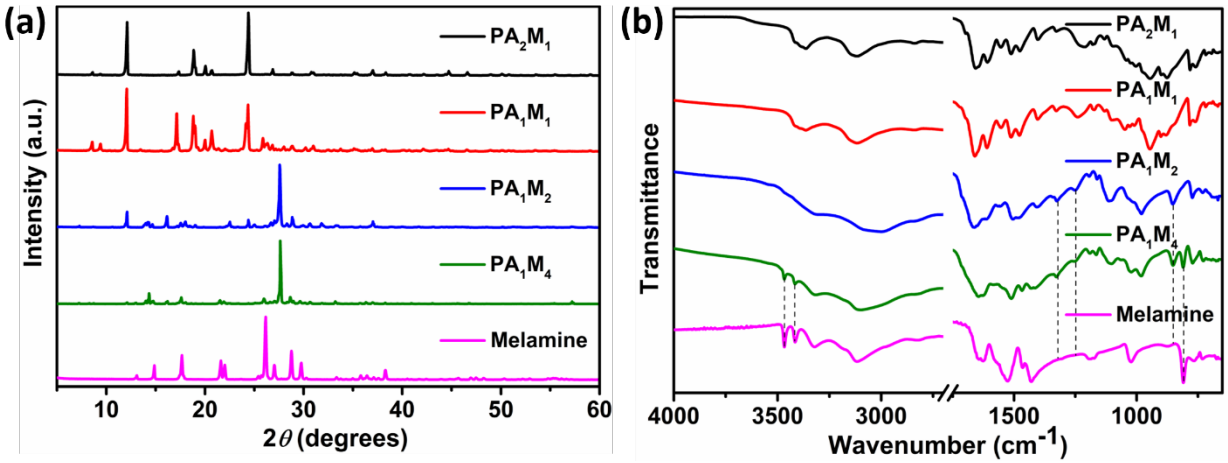

Fig. S2 Melamine and PA_xM_y (a) XRD patterns and (b) FTIR spectra. Patterns and spectra are offset for clarity.

XRD patterns of PA_1M_4, match almost perfectly with PA_1M_2 except its pattern shows low intense peaks at 17.7°, 21.6°, and 22° corresponding to the remaining non-reacting melamine units, further confirming PA_1M_2 and M superposition. FTIR spectroscopy measurements of the prepared crystals further confirm the establishment of an arrangement between phosphoric acid and melamine, as shown by the disappearance of the –NH stretching vibration of the amine groups within melamine units at 3468 and 3416 cm^{-1} as the amine hydrogen is connected either to another melamine (M) unit or PA. These vibrations are still present in PA_1M_4, further supporting the existence of non-reacting melamine units within the crystal. Another peak, located at 810 cm^{-1}, which correspond to the out-of-plane bending of melamine cyclic ring, also confirms the existence of the insulated melamine units. Moreover, two other peaks appear at 1250 (P=O) and 1324 cm^{-1} (P-O-C), provide an evidence for the existence of PA_1M_2 single-crystal in the mixture, indicating a superposition of two different single crystals as well.

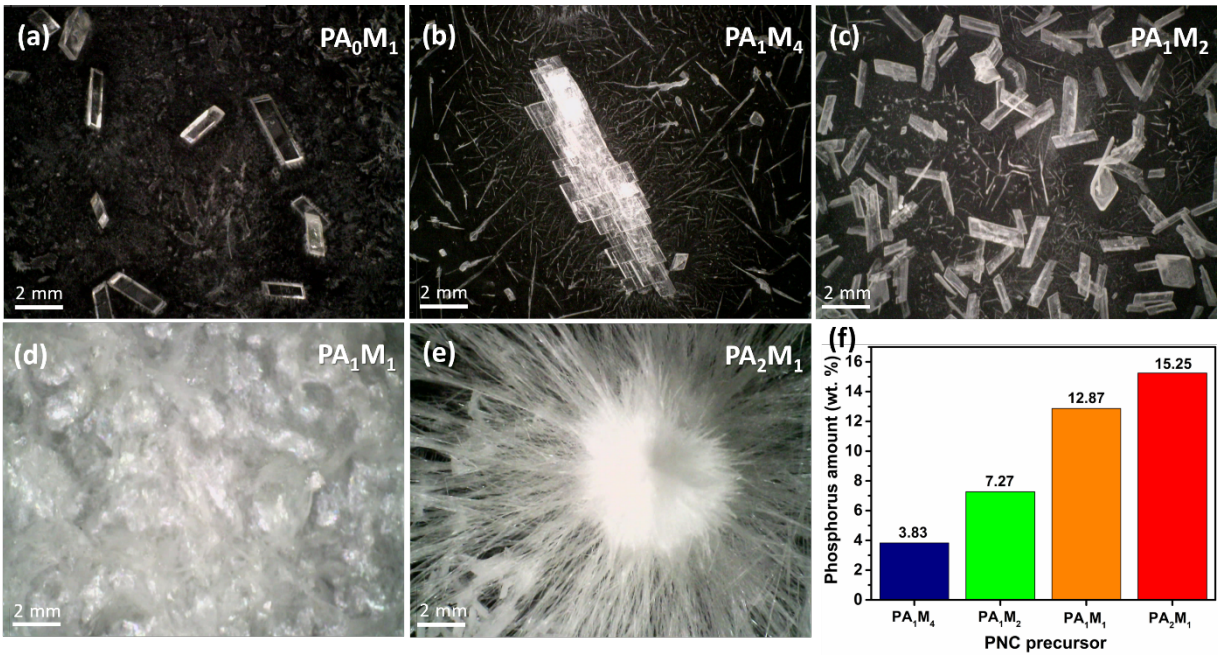

Fig. S3 (a–e) Optical microscopy images of PA_xM_y crystals, and (f) their phosphorus content in weight percentage, determined by ICP-OES.

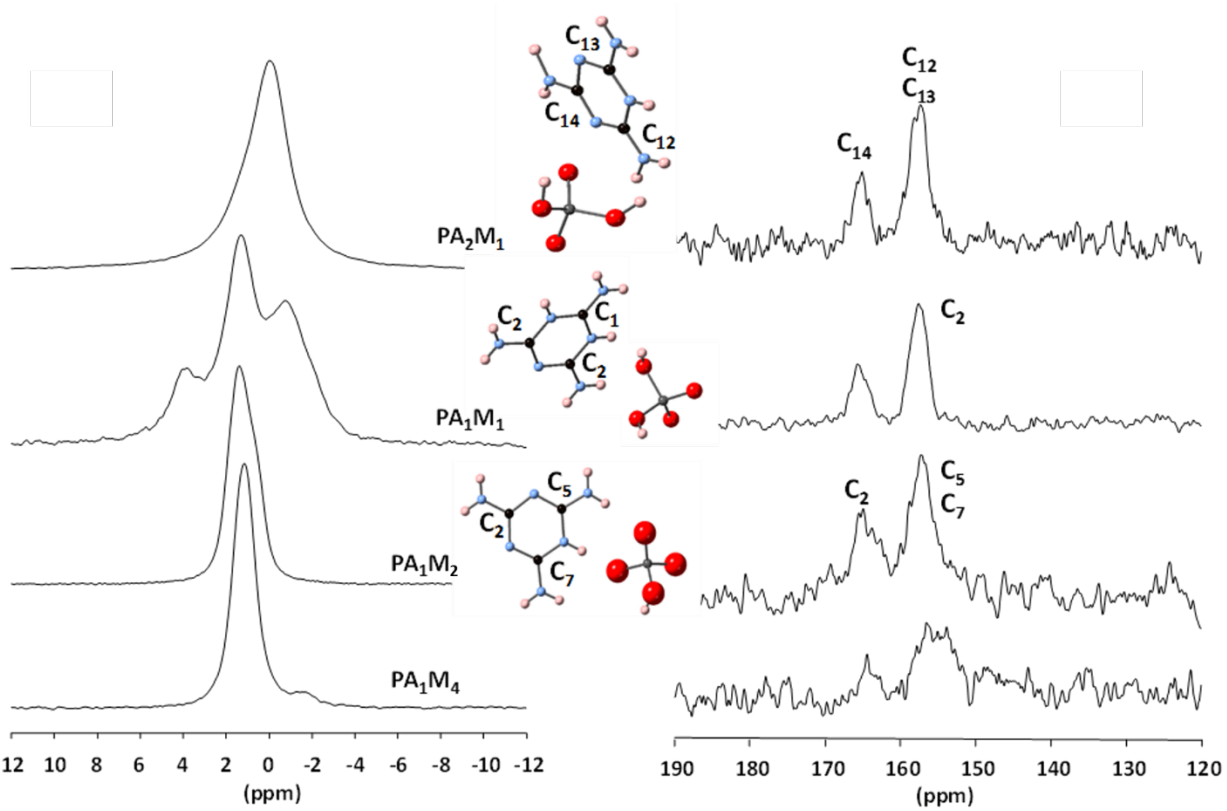

Fig. S4 (a) ^{31}P MAS and (b) ^{13}C CP MAS NMR spectra of PA_xM_y crystals. Assignment of the carbon signals is proposed according to NMR calculations on the crystalline structures.

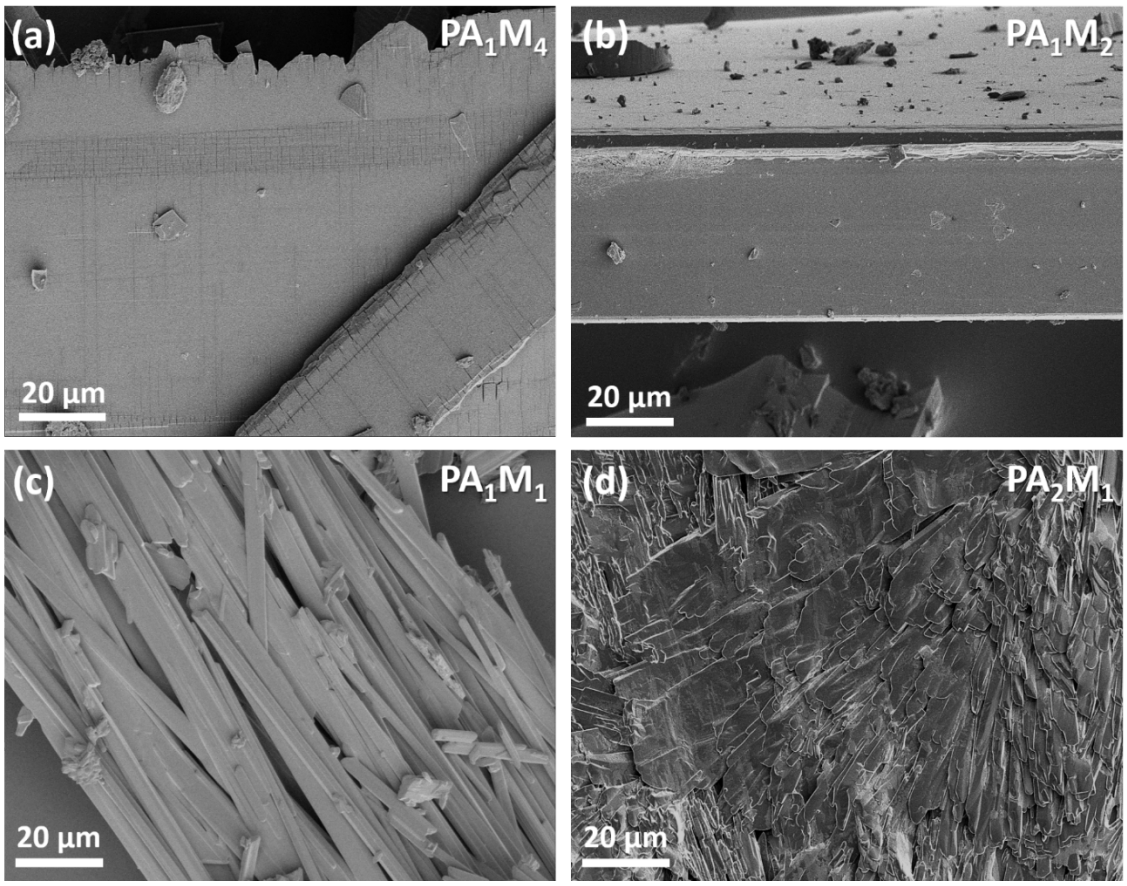

Fig. S5 SEM images of (a) PA_1M_4, (b) PA_1M_2, (c) PA_1M_1, and (d) PA_1M_1 crystals.

Table S3. EA and ICP data of PA_xM_y, which correspond to PA-M precursor molar ratio, melamine (M), and melamine single crystals (MSC) in wt. %.

Element	P	N	C	H	O
PA_2M_1	15.25	22.06	9.92	4.07	30.40
PA_1M_1	12.87	36.75	16.21	4.12	26.98
PA_1M_2	7.27	41.15	18.10	5.15	26.23
PA_1M_4	3.83	52.10	23.14	5.00	13.04
M	—	64.77	28.59	4.48	—
MSC	—	67.35	28.46	4.57	—

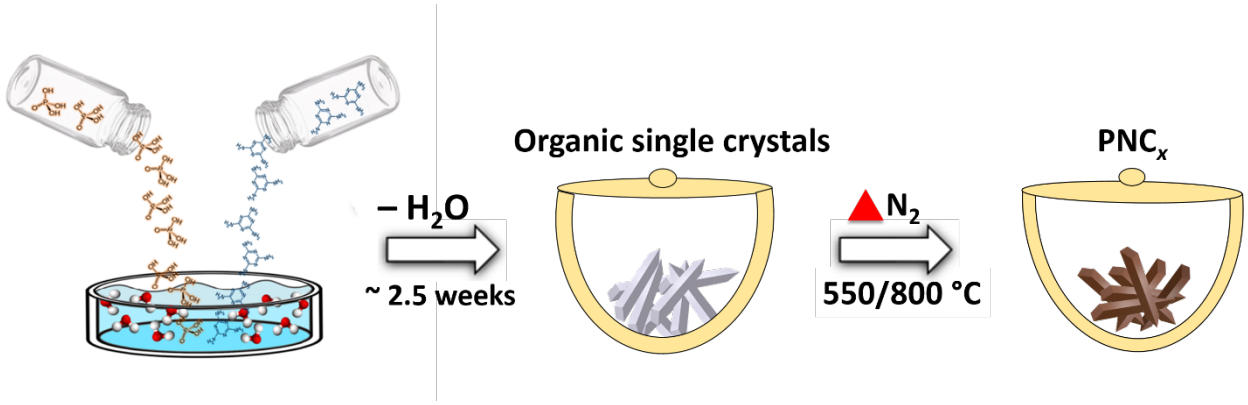

Fig. S6 Schematic representation of PNC$_x$ preparation.

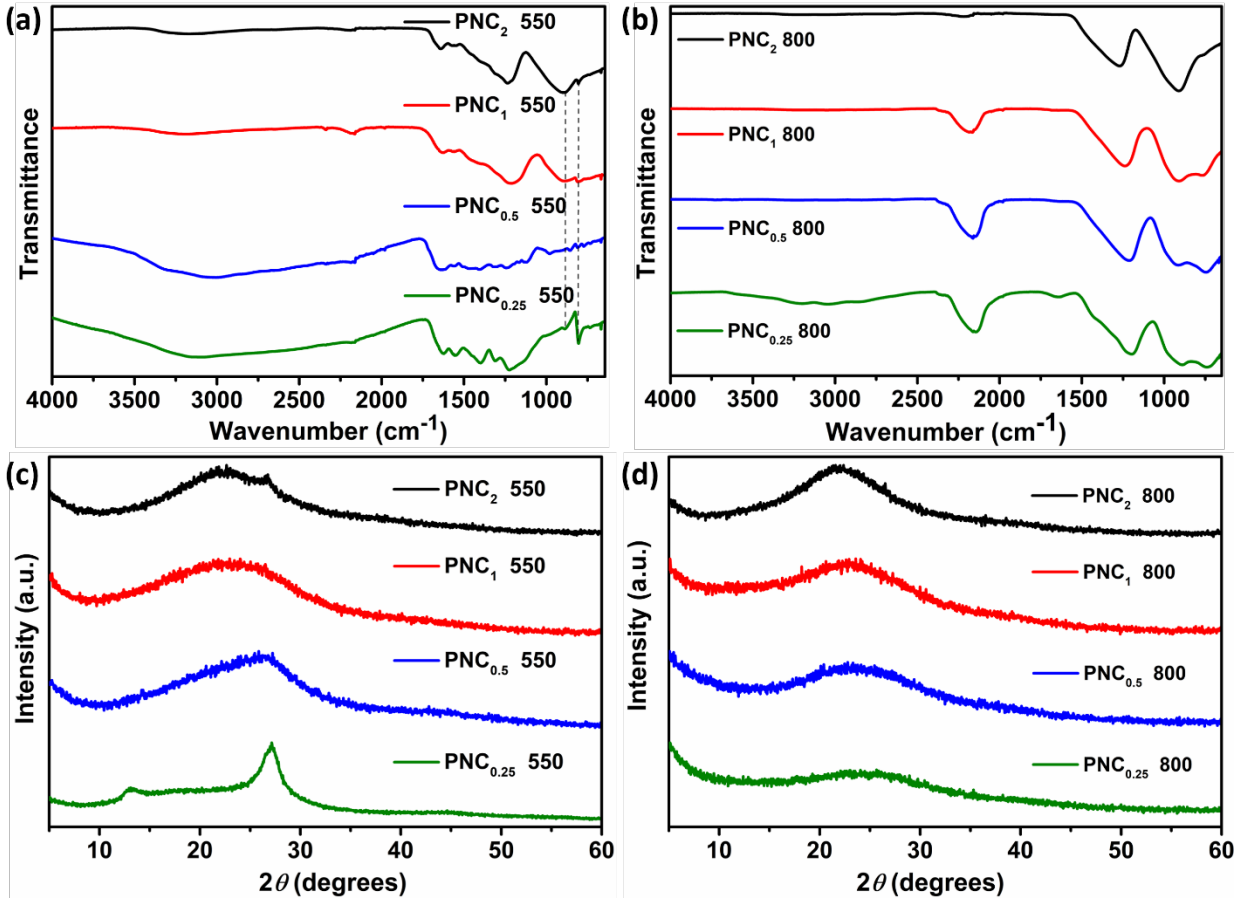

Fig. S7 FTIR spectra of (a) PNC$_x$ 550 and (b) PNC$_x$ 800. XRD patterns of (c) PNC$_x$ 550 and (d) PNC$_x$ 800. All spectra and patterns and are offset for clarity.

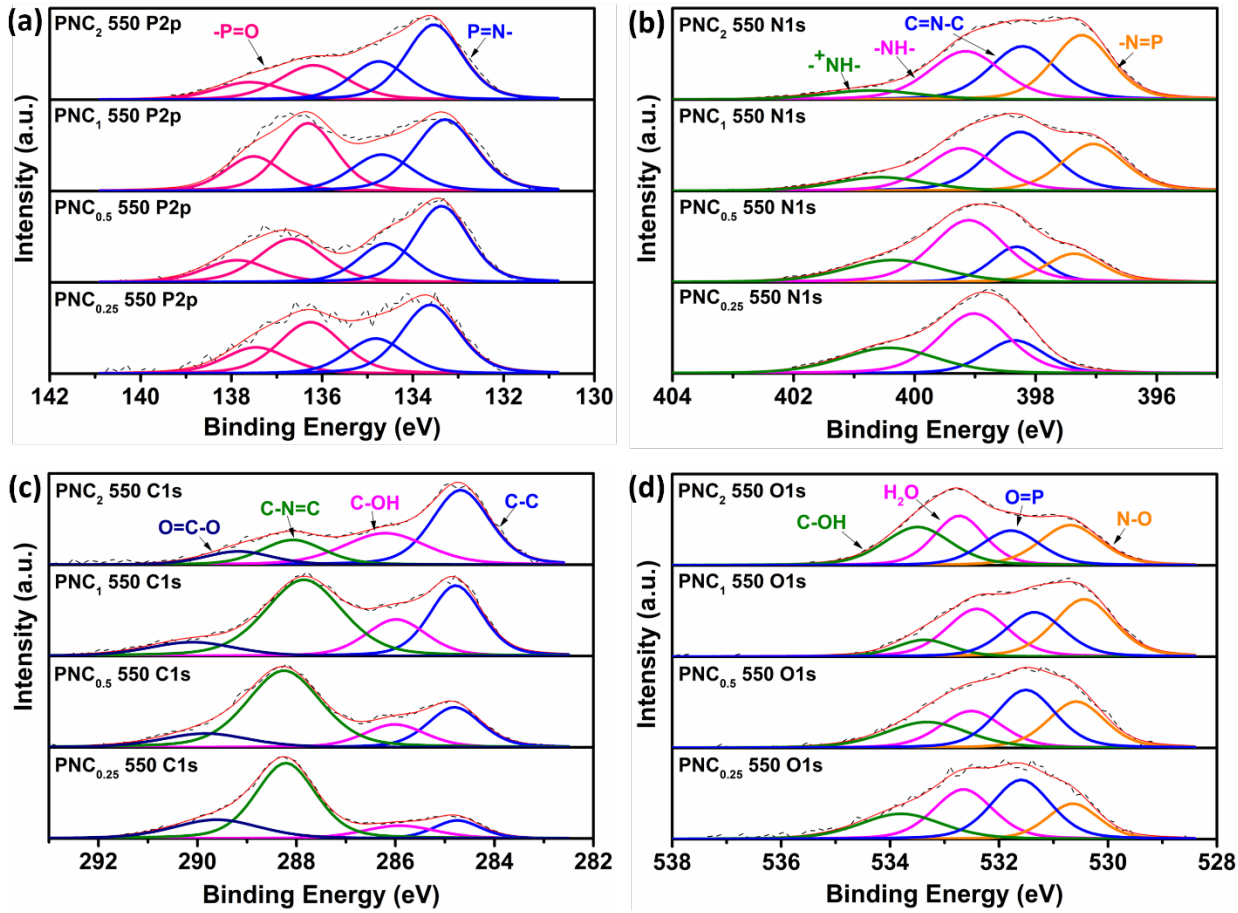

Fig. S8 PNC_x 550 XPS spectra for (a) $P2p_{3/2}$ and $P2p_{1/2}$, (b) N1s, (c) C1s, and (d) O1s.

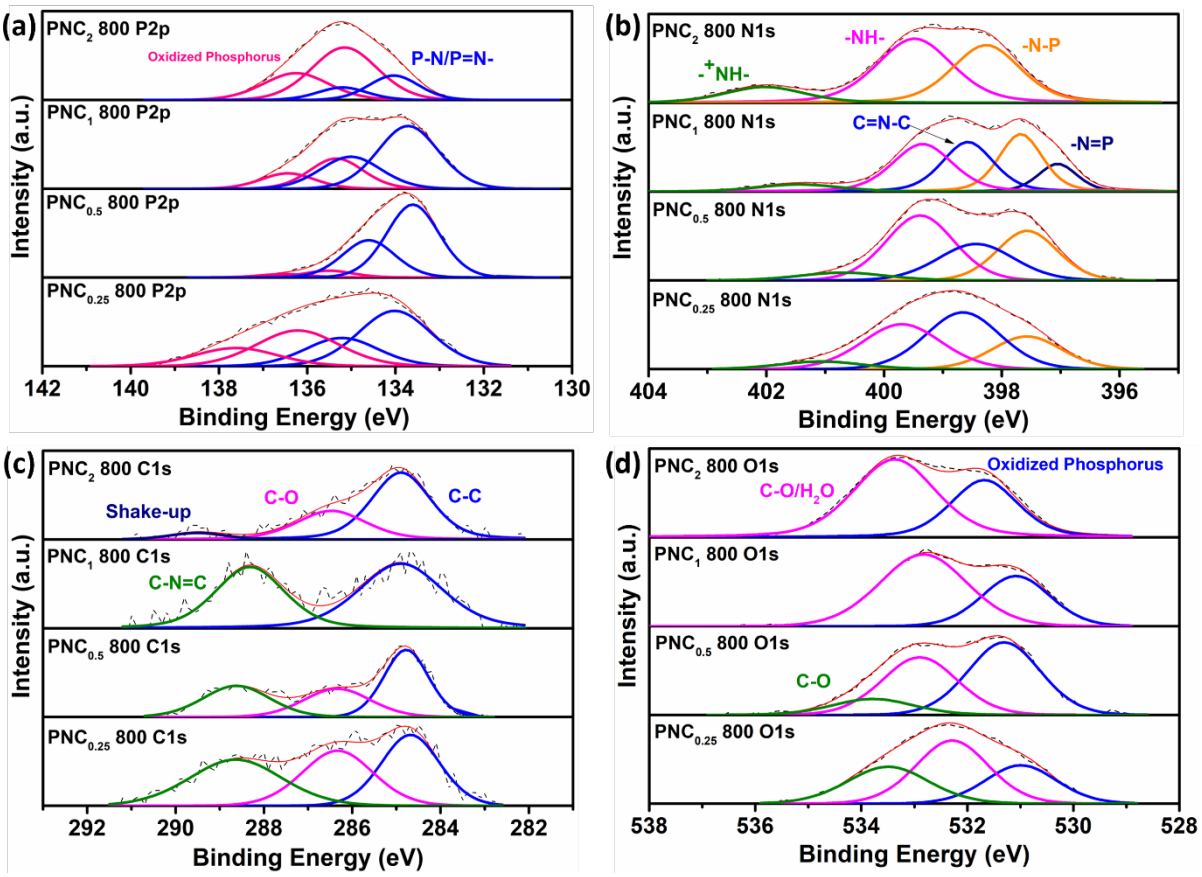

Fig. S9 PNC_x 800 XPS spectra for (a) $P2p_{3/2}$ and $P2p_{1/2}$, (b) N1s, (c) C1s, and (d) O1s.

The PNC_1 800 N1s spectrum expose five peaks at binding energies of: 397.0 (P=N), 397.7 (P-N), 398.6 (C-N=C), 399.4 (NH), and 401.5 eV (positively charged nitrogen atom).[5–8] The chemical contribution that belongs to the positively charged amine group, located at 402.3 eV in PNC_2 800, shifts to lower binding energies for lower *x* value due to larger amount of phosphanimine groups in the samples. Furthermore, the PNC_2 800 N1s spectrum shows only three nitrogen species at 397.5 (-N-P-), 398.9 (amine)[9], and 401.5 (-$^+$NH-) eV, suggesting the oxidation of the sp^2 C in C-N heterocycles. Both $PNC_{0.25}$ 800 and $PNC_{0.5}$ 800 C1s spectra show three species corresponding to C-C, C-O, and C-N=C chemical states, centered at 284.7, 286.3, and 288.6 eV, respectively.[10–12] PNC_1 800 presents only two chemical states attributed to C-C and C-N=C. The C1s spectrum of PNC_2 800 further confirms the low carbon content within the sample by the disappearance of the chemical state of C-N=C. Additionally, a new peak appears at 289.5 eV and may be caused by a shake-up π-π^* satellite.[13]

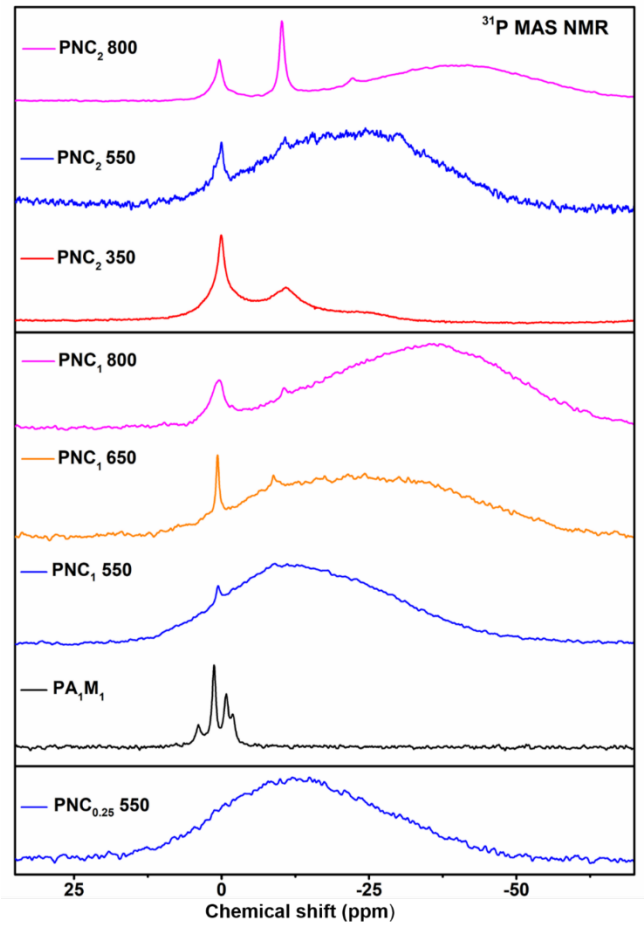

Fig. S10 ^{31}P MAS NMR of PA_1M_1 raw crystal (marked in black), PNC_2 calcined at 350 °C (marked in red), $PNC_{0.25}$, PNC_1, and PNC_2 calcined at 550 °C (marked in blue), PNC_1 calcined at 650 °C (marked in orange), and PNC_1, PNC_2 calcined at 800 °C (marked in magenta).

	δ (ppm)
P	-13,4
C1	164,4
C2	167,0
C3	162,9

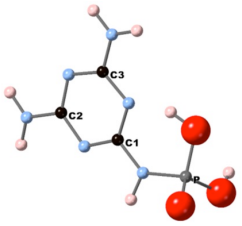

	δ (ppm)
P	-24,6
C1	166,0
C2	156,1
C3	157,0
C4	162,8
C5	156,4
C6	166,3
C7	166,4
C8	158,3
C9	166,5
C10	157,7
C11	166,5
C12	158,0

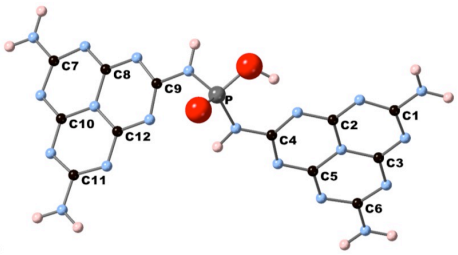

	δ (ppm)			δ (ppm)
P	-26,3			
C1	166,7		C13	169,9
C2	157,9		C14	157,4
C3	157,3		C15	159,1
C4	166,5		C16	166,3
C5	157,8		C17	158,6
C6	166,6		C18	166,7
C7	168,2		C19	166,7
C8	158,8		C20	158,7
C9	157,4		C21	167,0
C10	166,5		C22	157,8
C11	157,8		C23	167,3
C12	166,9		C24	157,2

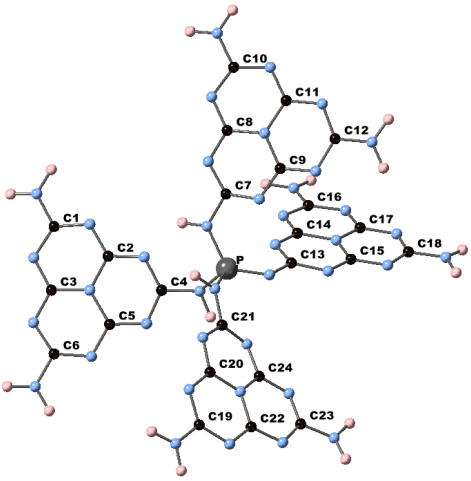

	δ (ppm)			δ (ppm)
P1	-28,2		C14	156,0
P2	-22,8		C15	157,2
P3	-1,9		C16	166,4
			C17	157,6
C1	166,5		C18	165,0
C2	158,1		C19	166,8
C3	157,3		C20	158,1
C4	165,2		C21	166,4
C5	157,9		C22	162,6
C6	166,6		C23	155,8
C7	167,6		C24	164,9
C8	158,7		C25	156,1
C9	157,4		C26	166,6
C10	166,3		C27	157,7
C11	157,9		C28	156,6
C12	166,6		C29	164,6
C13	169,2		C30	157,3

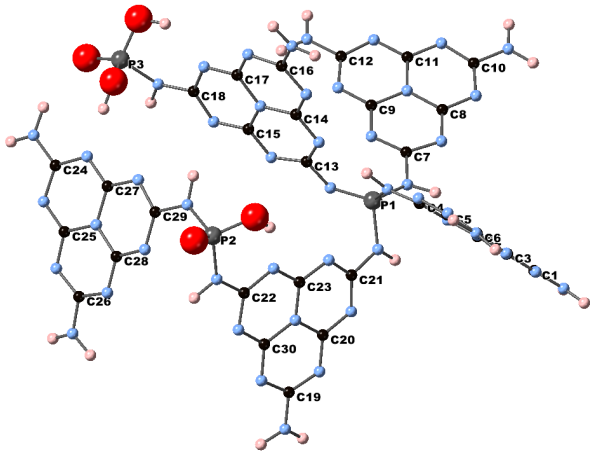

Fig. S11 Calculated ^{31}P and ^{13}C NMR parameters for a series of simples models with representative PO_xN_{4-x} environments with P linked to melamine or melem entities.

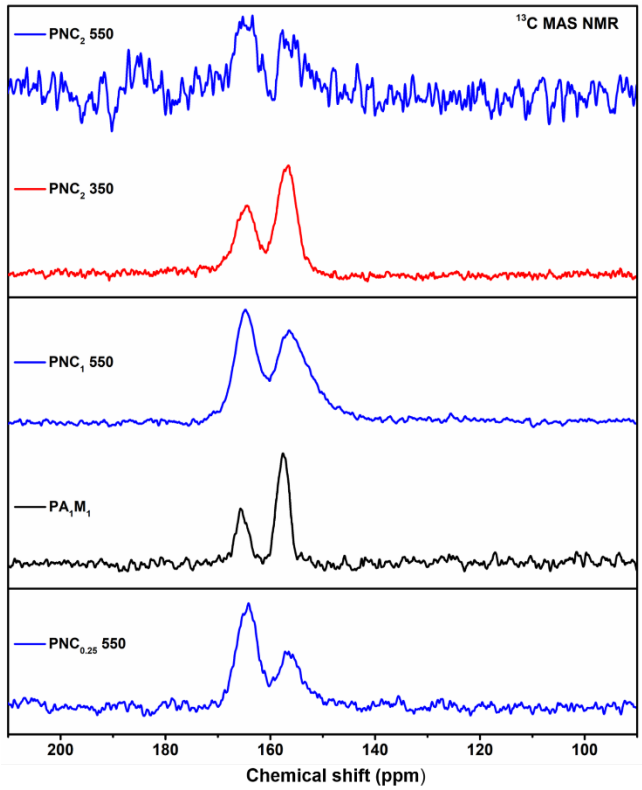

Fig. S12 ^{13}C CP MAS NMR spectra of PA_1M_1 crystal (marked in black), $PNC_{0.25}$, PNC_1, and PNC_2 synthesized at 550 °C (marked in blue), and PNC_2 synthesized at 350 °C (marked in red).

Table S4. EA and ICP of PNC_x (x is the PA:M molar ratio) calcined at 550 °C. All values are presented in wt. %.

Element	P	N	C	H	O
PNC_2 550	35.04	31.30	4.66	0.93	8.80
PNC_1 550	27.62	41.73	11.90	2.20	13.06
$PNC_{0.5}$ 550	16.74	48.04	21.69	1.61	7.43
$PNC_{0.25}$ 550	11.10	54.40	26.80	1.81	5.21

Table S5. EA and ICP of PNC_x (x is the PA:M molar ratio) calcined at 800 °C. All values are presented in wt. %.

Element	P	N	C	H	O
PNC_2 800	51.34	25.86	0.87	0.93	1.95
PNC_1 800	47.46	39.08	4.78	0.20	9.51
$PNC_{0.5}$ 800	48.47	40.58	5.46	0.25	4.81
$PNC_{0.25}$ 800	43.34	32.81	5.30	0.73	8.19

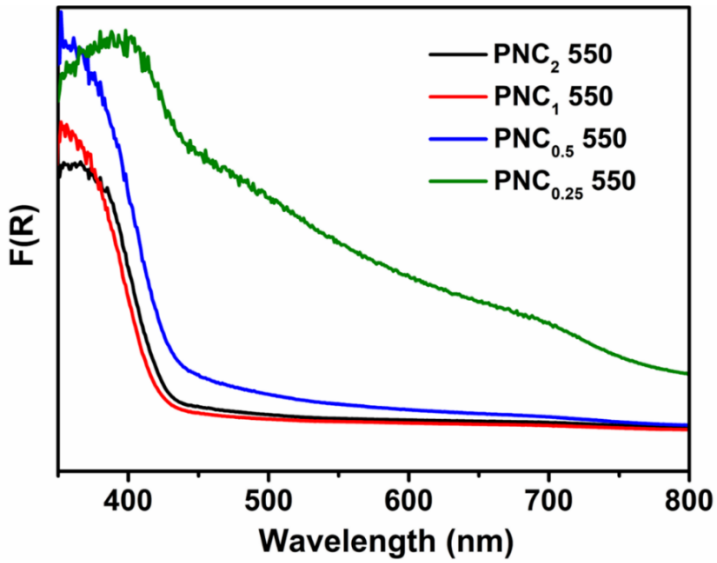

Fig. S13 PNC_x 550 UV-vis spectra. F(R) is Kubelka-Munk function that represents absorbance based on a reflectance measurement.

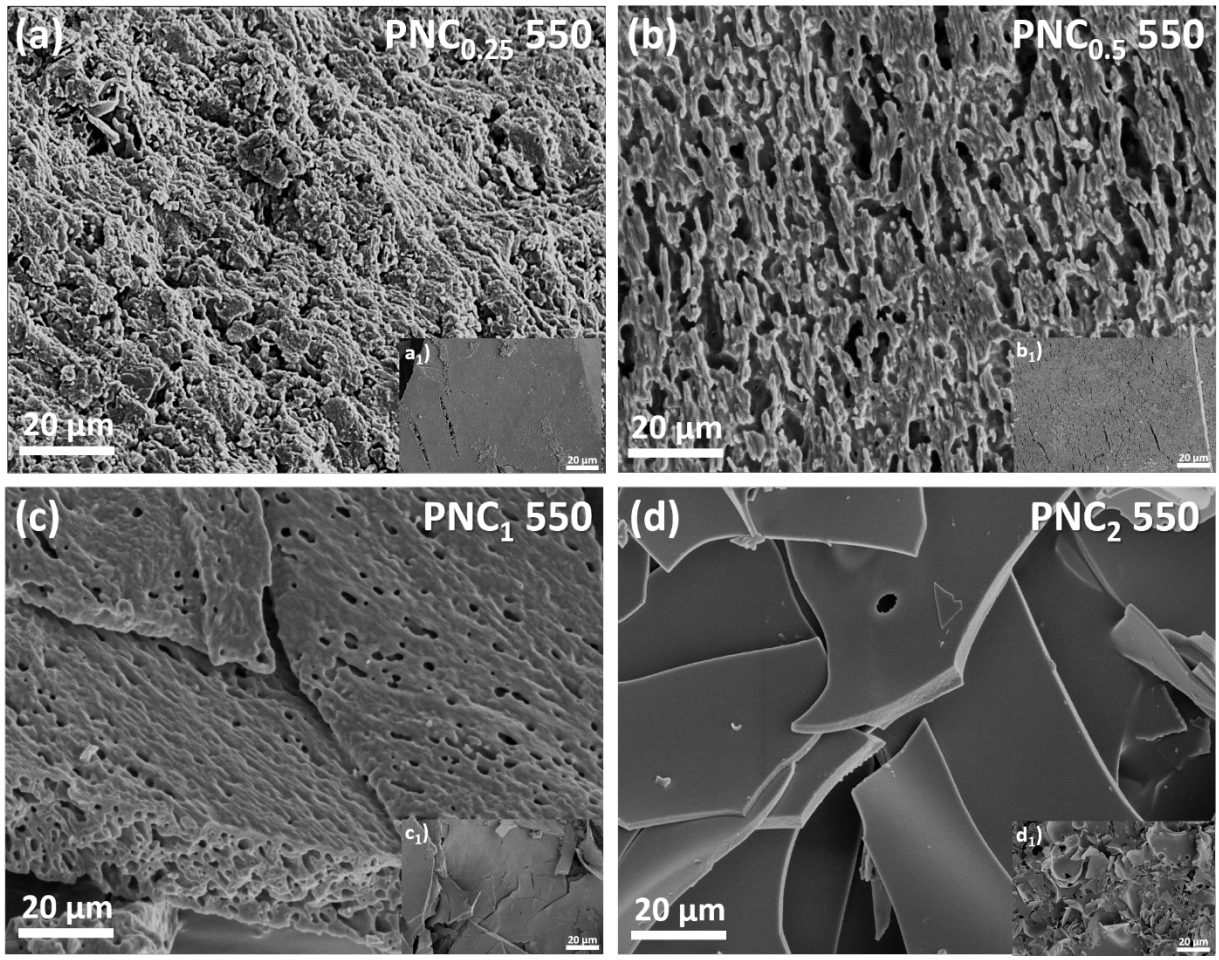

Fig. S14 SEM images of PNC_x 550 materials.

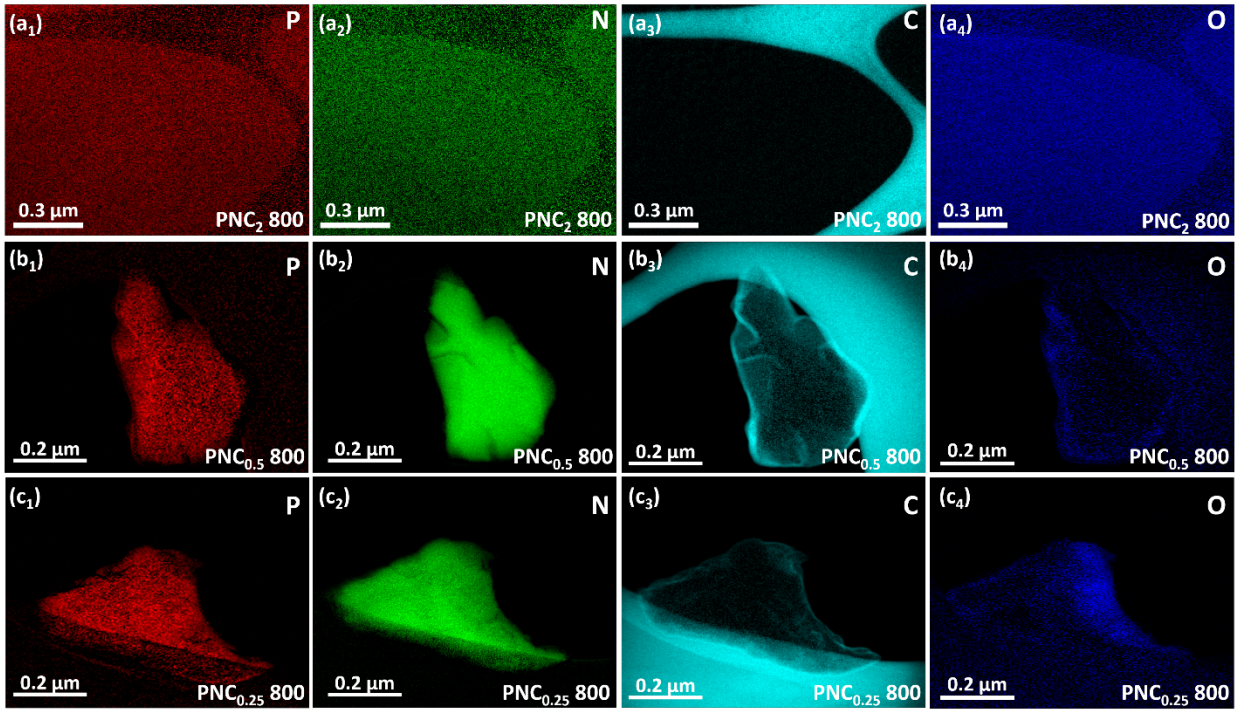

Fig. S15 EFTEM of (a_x) PNC_2 800, (b_x) $PNC_{0.5}$ 800 and (c_x) $PNC_{0.25}$ 800 (x = 1, 2, 3, 4 for phosphorus, nitrogen, carbon, and oxygen, respectively) supported on an ultrathin carbon grid.

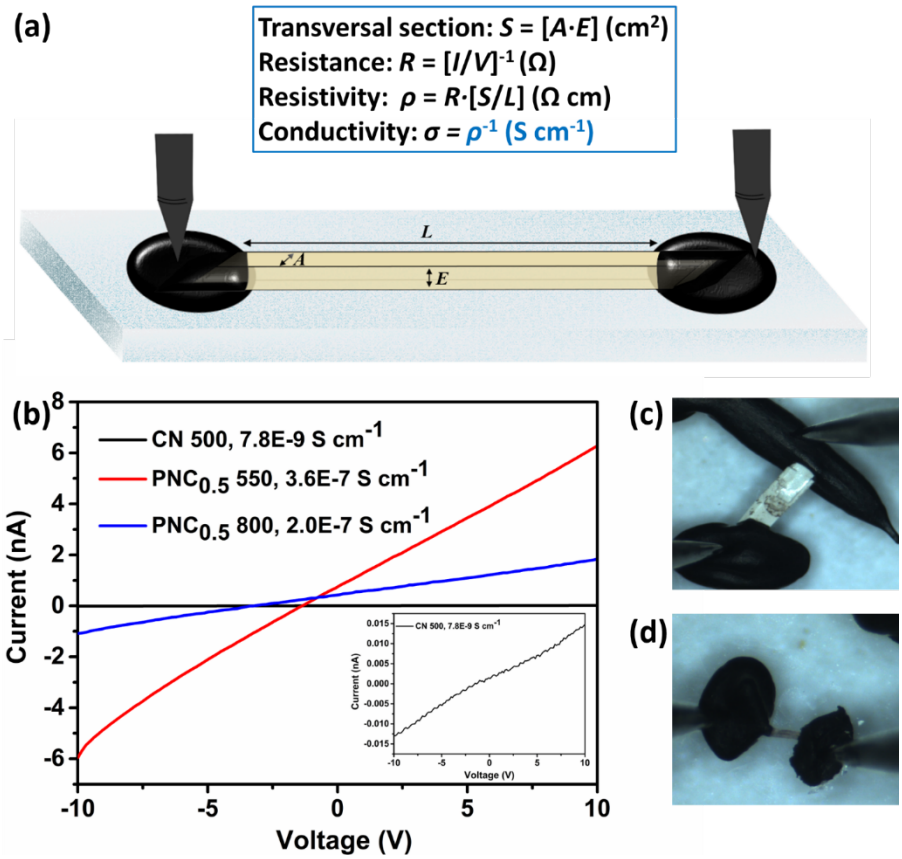

Fig. S16 Electrical conductivity measurements. a) Illustration of electrical conductivity measurement setup, (b) *I–V* plots of $PNC_{0.5}$ 550, $PNC_{0.5}$ 800, optical images of (c) $PNC_{0.5}$ 550, and (d) $PNC_{0.5}$ 800 while placing between two conductive tungsten probes. Calculated conductivity values: σ(CN 500) = 7.8×10^{-9} S cm^{-1}, σ($PNC_{0.5}$ 550) = 3.6×10^{-7} S cm^{-1}, and σ($PNC_{0.5}$ 800) = 2.0×10^{-7} S cm^{-1}.

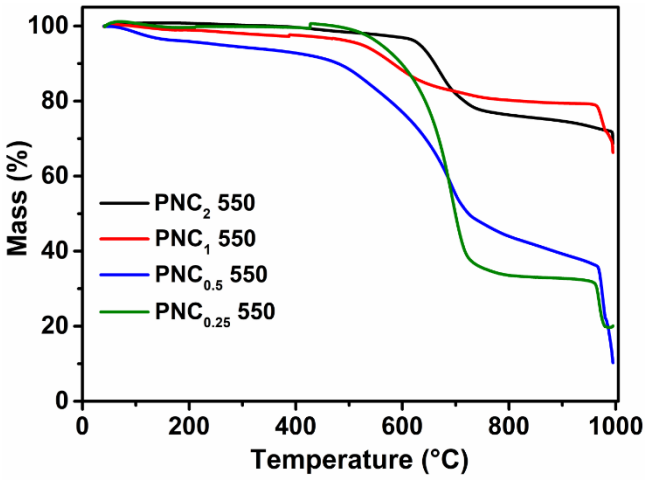

Fig. S17 Thermal gravimetric analysis (TGA) curves of PNC_x 550 under air.

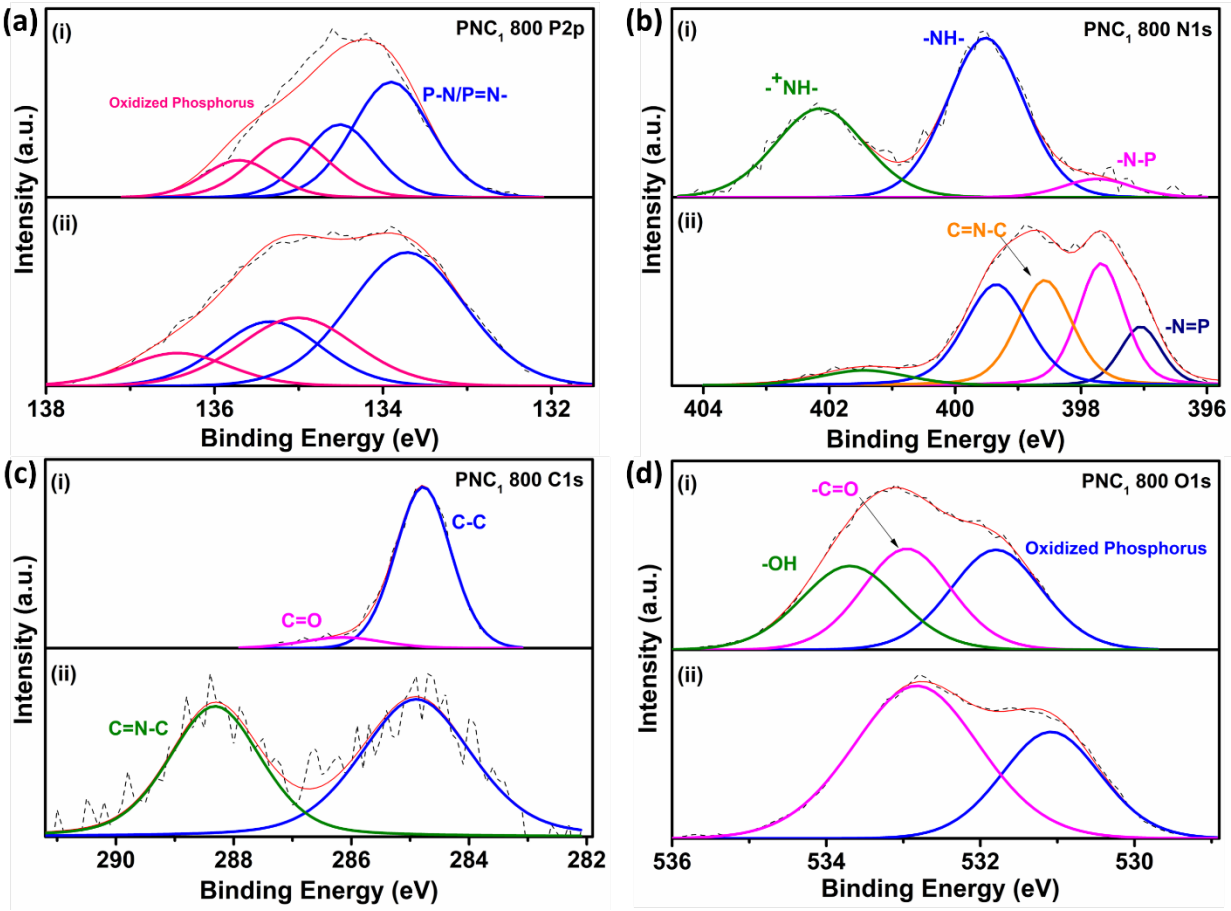

Fig. S18 PNC_1 800 XPS spectra for (a) P2p, (b) N1s, (c) C1s, and (d) O1s: after (i) and before (ii) burning under visible fire.

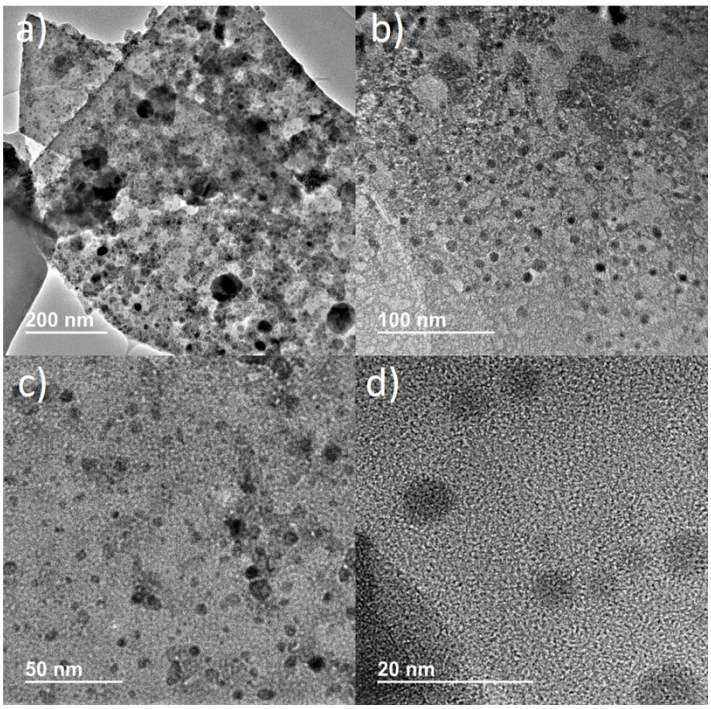

Fig. S19 HRTEM images of Ni/PNC$_{0.5}$ 800 at different magnifications.

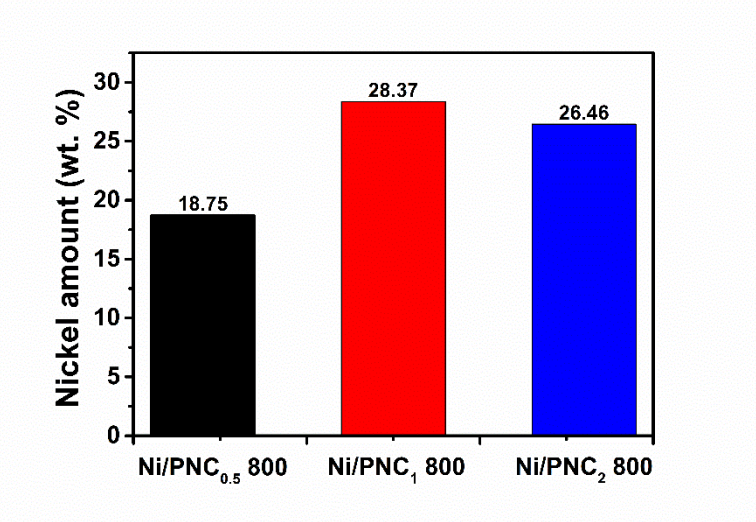

Fig. S20 Ni/PNC$_x$ 800 nickel content in weight percentage (measeured using ICP-OES).

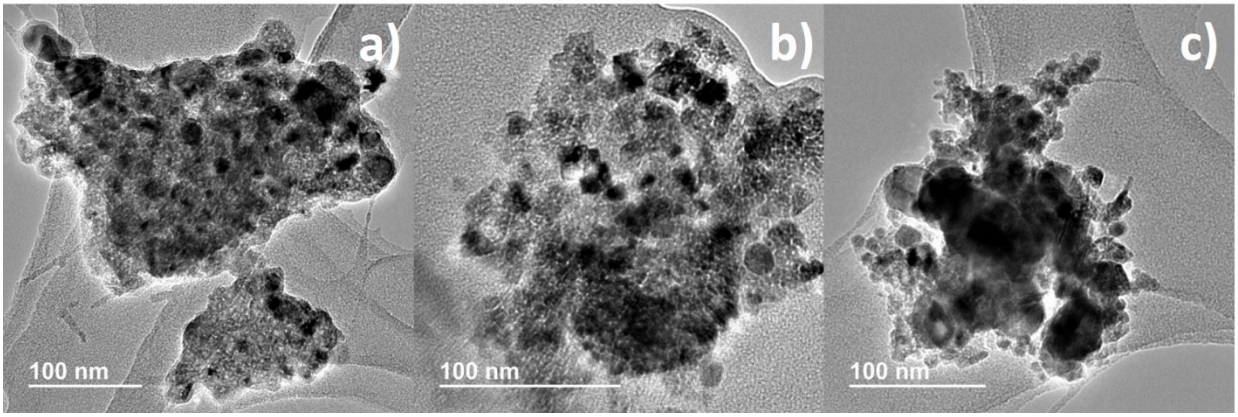

Fig. S21 HRTEM images of $Ni/PNC_{0.5}$ (a), Ni/PNC_1 (b), and Ni/PNC_2 (c) after 20 h methanation reaction at 400 °C.

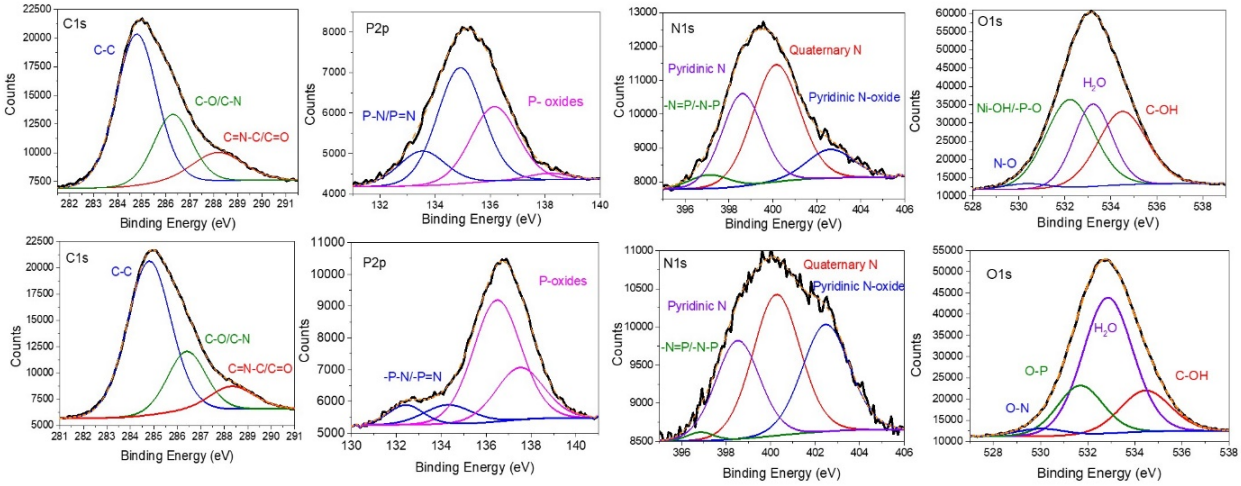

Fig. S22 XPS of $PNC_{0.5}$ 800 before (top panels) and after reaction (bottom panels).

References

1 D. J. A. De Ridder, K. Goubitz, V. Brodski, R. Peschar and H. Schenk, *Helv. Chim. Acta*, 2004, **87**, 1894–1905.

2 X. Li, S. Feng, F. Wang, Q. Ma and M.-L. Zhu, *Acta Crystallogr. Sect. E Struct. Reports Online*, 2010, **66**, o239–o240.

3 S. T. Huang, G. L. Wang, N. B. Li and H. Q. Luo, *RSC Adv.*, 2012, **2**, 10948–10954.

4 P. Li, H. D. Arman, H. Wang, L. Weng, K. Alfooty, R. F. Angawi and B. Chen, *Cryst. Growth Des.*, 2015, **15**, 1871–1875.

5 A. Fukushima, A. Hayashi, H. Yamamura and M. Tatsumisago, *Solid State Ionics*, 2017, **304**, 85–89.

6 J. Wu, S. Yang, J. Li, Y. Yang, G. Wang, X. Bu, P. He, J. Sun, J. Yang, Y. Deng, G. Ding and X. Xie, *Adv. Opt. Mater.*, 2016, **4**, 2095–2101.

7 W. Liang, J. Lei and C. R. Martin, *Synth. Met.*, 1992, **52**, 227–239.

8 M. L. Kantam, M. Roy, S. Roy, B. Sreedhar and R. Lal De, *Catal. Commun.*, 2008, **9**, 2226–2230.

9 J. Yue and A. J. Epstein, *Macromolecules*, 1991, **24**, 4441–4445.

10 P. Goli, S. Legedza, A. Dhar, R. Salgado, J. Renteria and A. A. Balandin, *J. Power Sources*, 2014, **248**, 37–43.

11 G. Wulff, H. Schmidt and L. Zhu, *Macromol. Chem. Phys.*, 1999, **200**, 774–782.

12 J. Xu, L. Zhang, R. Shi and Y. Zhu, *J. Mater. Chem. A*, 2013, **1**, 14766.

13 L. Tao, Q. Wang, S. Dou, Z. Ma, J. Huo, S. Wang and L. Dai, *Chem. Commun.*, 2016, **52**, 2764–2767.